

---

# MODELLING EXTINCTION IN STELLAR POPULATIONS

---

M.Phil. thesis

**Alexander Lisboa-Wright**

---

Astrophysics Research Institute, Liverpool John Moores University  
September 2019

## **Abstract**

## Units & Terminology

Unless stated otherwise, all quantities will be described in CGS units (masses in grams, lengths in centimetres, times in seconds, energies in ergs).

In this project, the notation  $\log(x)$  represents the logarithm of  $x$  to the base 10. The natural logarithm of  $x$  will be expressed as  $\ln(x)$ .

$$\begin{aligned}
 M &: \text{mass} \\
 M_{\odot} &= 1.989 \times 10^{33} \text{ g} : \text{solar mass} \\
 L &: \text{luminosity} \\
 L_{\odot} &= 3.842 \times 10^{33} \text{ erg s}^{-1} : \text{solar luminosity} \\
 g &: \text{gravity} \\
 R &: \text{radius} \\
 G &= 6.6723 \times 10^{-8} \text{ cm}^3 \text{ g}^{-1} \text{ s}^{-2} : \text{gravitational constant} \\
 \sigma_{\text{SB}} &= 5.678 \times 10^{-5} \text{ erg cm}^{-2} \text{ K}^{-4} \text{ s}^{-1} : \text{Stefan-Boltzmann constant}
 \end{aligned}$$

# Chapter 1

## Introduction

### 1.1 Motivation

Stellar populations, most prominently star clusters, represent one of the richest sources of information in the known universe. Stars within clusters are generally believed to have formed in a single brief time-period, making their ages essentially the same. Furthermore, because the stars are clustered in the night sky, the regions of space through which the light from each star travels to reach the same telescope are far more likely to be very similar to the relevant regions for all the other cluster stars, meaning the effects of the interstellar environment on the light is more likely to be the same for all the stars. This greatly simplifies the observational corrections required to analyse the physics of the cluster and the individual stars. This allows for direct comparison with current theoretical models, allowing detailed study of the physics stellar magnetic fields, rotation and internal mixing, among others. Determining the age of a cluster is an extremely powerful tool for this, especially for stars too far away to observe their physical properties with high precision.\*\*\*\* \*\*understanding of galactic history, elemental abundances, etc.

As the light emitted from a star travels towards a distant observer, its intensity, or flux,  $F$  decreases with distance  $d$  via an inverse-square law:

$$F = \frac{L}{4\pi d^2} \tag{1.1}$$

where  $L$  is the star's luminosity, which is an intrinsic property of the star (i.e., independent of the observer). Equation 1.1 is a natural consequence of the same light wave expanding outwards from its source into a progressively larger spherical volume of empty space.

However, the interstellar medium is not a perfect vacuum. It contains many different structures, such as diffuse gas clouds, that can absorb or scatter light passing through, depending on the wavelength of the incoming photons, the spacing between the individual atoms (i.e., the density of the medium) and the quantum levels in the atoms occupied by their electrons. These absorption and scattering events are known

as interstellar extinction. For a given source, its interstellar extinction coefficient represents the sum of the effects of all extinction events along the line-of-sight between the source and the observer.

Interstellar extinction preferentially affects light at shorter (i.e., bluer) wavelengths. Therefore, the effect of extinction is sometimes referred to as “reddening”, despite the fact that this term is also applied to a related, but distinct, quantity (see Section 2.2). Therefore, it should be expected that sources with proportionally higher fluxes at shorter wavelengths are most affected by extinction.

The goal of this project is to attempt to use analytic functions to model the variation of the extinction coefficients in multiple filter systems, across as large a range of stellar types as possible, with the ultimate goal of using this simplification of the variations to determine the differences in the estimated optimal ages, elemental abundances (known collectively in astronomy as metallicity) and  $A_V$  values of stellar populations (i.e., star clusters) from the current standard method for simulating extinction. If such differences exist and if they are of significant size, it could cause a recalculation of the properties of observed star clusters. This could potentially cause a reinterpretation of these clusters’ history, including where and when they formed in the Milky Way and the chemical enrichment of the gas that formed their stars.

## 1.2 Observational constraints

No telescope can view the sky at all spectral wavelengths - it would be wholly impractical due to the sheer number of sources across the spectrum, as well as the fact that telescope resolution depends on the wavelength of the incoming light. Therefore, modern telescopes are equipped with a system of filters or bands, which allow only light within a narrow range of wavelengths. In a filter system, the individual filters are designed to operate best at different wavelengths. The system will be therefore have the following properties:

- the filters cover a much wider range of spectral wavelengths than a single filter would alone; this is used to observe sources at different wavelengths to determine its spectral colour (see Section ).
- The filters are designed such that the range of wavelengths in which they can best detect incoming light overlap with their neighbours, as shown in Figures 1.1-1.4. This ensures that there are no wavelength gaps in which incoming light cannot be detected. This is particularly important for quantum line emission, which occurs only at specific wavelengths for particular electron occupancy levels (see Section for exceptions relevant to this case). One of the most prominent case of astrophysical line emission is that of  $H\alpha$ , in which the electron in a neutral hydrogen atom transitions from the  $n = 3$  to the  $n = 2$  quantum occupation state, emitting a photon with a wavelength of 656 nm, which is in the red part of the visible spectrum.

\*\*\*\*Filters - Johnson, ACS, WFC/UVIS, Gaia

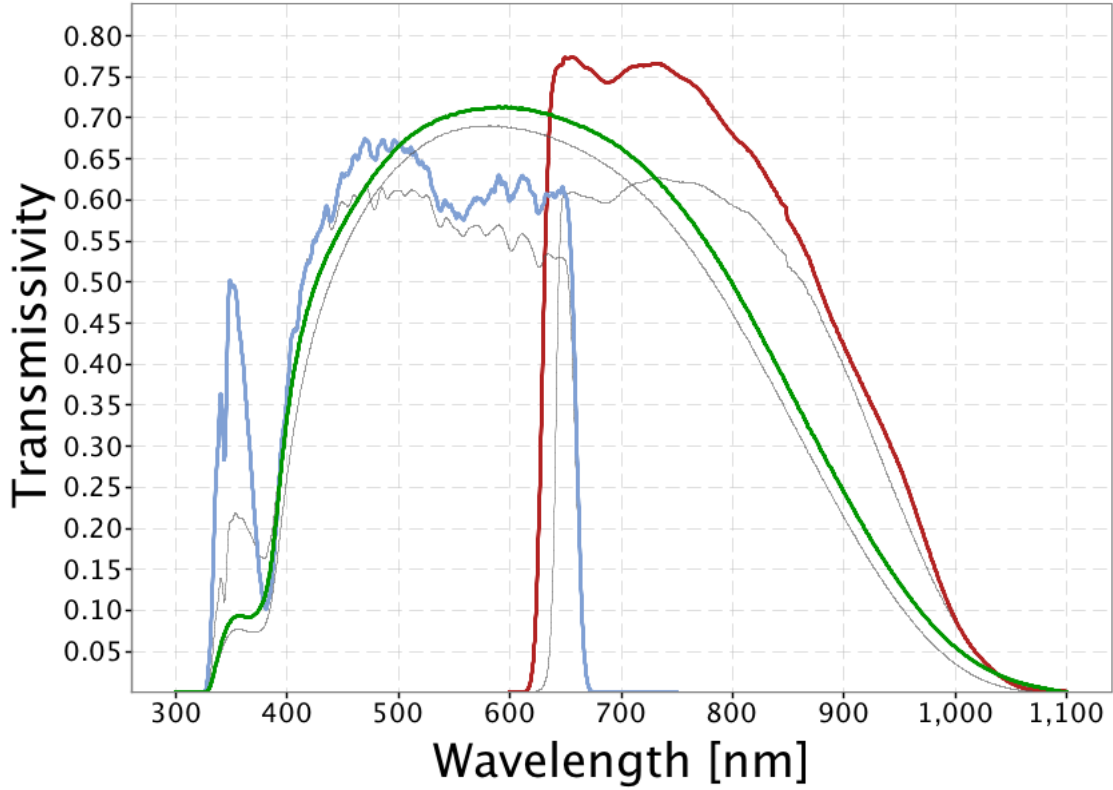


Figure 1.1: Filter response functions for Gaia photometric filters. Source: [https://www.cosmos.esa.int/web/gaia/iow\\_20180316](https://www.cosmos.esa.int/web/gaia/iow_20180316)

The standard treatment of extinction is to apply a single constant value of the extinction coefficient for a given filter  $X$ , denoted in the literature by  $A_X$ . For wavelengths in or close to the optical spectral range, this quantity is usually expressed as a fixed ratio of the (constant) coefficient value in the Johnson- $V$  filter, the standard visual comparison filter.

In this project, three broad-band filter systems were employed. These are the Advanced Camera for Surveys (ACS) and the Ultraviolet Imaging Spectrograph channel of the Wide-Field Camera 3 (WFC3/UVIS), both mounted on the Hubble Space Telescope (HST), and the single set of three broadband filters mounted on the Gaia space observatory (Jordi et al., 2010).

Filters thus\*\*\*\* present a challenge when trying to determine stellar spectra accurately. This task is further complicated by the fact that, even in the wavelength range where a filter does detect incoming flux, the fraction of light it detects, known as the transmittance, is not uniform across the range. The transmittance as a function of wavelength is known as a transmission curve, bandpass or filter response function. Examples of response functions for some\*\*\*\* of the filters employed in this project are

System	Filter	Central wavelength / Å	FWHM / Å
ACS	F435W	4760	729
	F475W	5000	986
	F555W	5060	841
	F606W	6690	1566
	F625W	6480	978
	F775W	7320	1017
	F814W	7460	1657
WFC3	F218W	2175	300
	F225W	2250	500
	F275W	2750	500
	F300X		2775
	F336W	3375	550
	F390W	3900	1000
	F438W	4320	695
	F475W	4750	1520
	F555W	5410	1605
	F606W	5956	2340
	F625W	6250	1550
	F775W	7760	1470
	F814W	8353	2555
Gaia	G	6730	4400
	G <sub>bp</sub>	5320	2530
	G <sub>rp</sub>	7970	2960

Table 1.1: Basic properties of the filters employed in this project.

shown in Figure 1.4. By comparing these with the filters' information in Table 1.1, it can be seen that the exact shape of the response function could have a significant impact on the observed spectrum if not taken into account. The values in the column labelled 'FWHM' represents the full width at half-maximum. In this case, it is defined as the difference between the lowest and highest wavelength values at which the transmittance value is half of its maximum value for the filter, typically assuming the response function can be approximated as a Gaussian distribution centred on the central wavelength. The FWHM acts as an approximate measure of the wavelength range within which the filter can reliably be used for observations.

The wavelengths of light visible to an average human eye are in the range 3800-7400 Å. Hence, the filters used here cover wavelengths from the soft-ultraviolet (soft-UV) to the near-infrared (NIR), including all visible wavelengths.

### 1.3 Basics of stellar evolution

While observations can reveal properties of individual stars and stellar populations more generally, the significance of these properties can only be gained by understanding the underlying physical processes and structure of the stars themselves.

\*\*\*\*It can be seen that all stars lie on a single, complicated line, known as an isochrone. Isochrones for different population ages and metallicities are calculated using theoretical stellar models for the largest possible spread of initial stellar masses. An isochrone in the HR diagram has a number of distinct features:

- Most stars, including the coolest and least-luminous ones, follow a tight pattern of luminosity increasing with temperature. This is known as the main sequence (MS)
- This pattern stops as the luminosity continues to increase slowly but with decreasing temperature. The end of the MS is called the main-sequence turn-off (MSTO), which is followed by the sub-giant branch (SGB).
- After the SGB, the gradient becomes much steeper, with temperature decreasing and luminosity rapidly increasing. This is the red-giant branch (RGB).
- At the tip of the RGB, stars start becoming fainter and their temperatures increase. Eventually, there is a sequence of stars with near-constant luminosity but a range of effective temperatures. This is the horizontal branch (HB).
- After the horizontal branch, there is again a rapid increase in luminosity accompanied by a slow decrease in temperature. This is the asymptotic giant branch (AGB).

In the main sequence, nuclear fusion occurs in the core and any products must be subjected to mixing effects to reach the atmosphere. Since stellar interiors are physically fluid, heavier nuclei, which are more dense, preferentially gather in regions



close to the star's centre of gravity. Therefore, processes such as convection, thermohaline mixing and radiative levitation are required to induce a noticeable change in surface composition. However, these processes require certain physical conditions on local scales, if they are to be sustained for long enough to induce a visible change in the stellar spectrum.

On the main-sequence, only low-mass stars ( $M_* \lesssim 0.38M_\odot$ ) (Baraffe & Chabrier, 2018) have fully-convective interiors. Massive ( $M_* \gtrsim 1.5M_\odot$ ) stars have convective cores, but radiative envelopes. Intermediate-mass stars, including the Sun, have radiative cores and convective envelopes. Since regions in which energy transport is dominated by radiative effects are stable against convection, stars with masses greater than  $0.38M_\odot$  are highly unlikely to show large changes in atmospheric composition along the main sequence. However, the fully-convective lower-mass stars are able to do so. Therefore, the faintest and reddest parts of the main sequence are most likely to have atmospheres enriched with metals, which would be confined in the cores of more massive stars. These enriched atmospheres are therefore highly sensitive to the overall metallicity of the original gas cloud in which the star, and its parent cluster if applicable, formed\*\*\*\*.

$$\nabla_{\text{rad}} = \frac{3\kappa LP}{16\pi acGmT^4} \quad (1.2)$$

To illustrate, let us consider a bubble of gaseous material in pressure-equilibrium with its surroundings and represent mixing as a significant change in the bubble's (radial) position on a significant time-scale, arising from small differences in the remaining 3 thermodynamic quantities between the bubble and its surroundings. For a non-rotating star, using a simple linear approach, together with the Archimedes principle, gives a set of 4 homogeneous differential equations for the (small) differences in  $P$ ,  $T$ ,  $\mu$  and  $r$  (Equations (3.1)-(3.4) in Salaris & Cassisi (2017)). If  $\Delta x_i$  are the differences in the 4 parameters, taking the ansatz form  $\Delta x_i = B_i e^{nt}$  allows for a solution as a 3rd-order polynomial in  $n$  (Equation (3.5) in Salaris & Cassisi (2017)), if the determinant of the relevant matrix (dependent of the values of the  $B_i$ ) is zero. The Routh-Hurwitz stability criterion can then be applied to this polynomial to give a general solution for  $n$ . For a physically-unstable solution, the exponent in the  $\Delta x_i$  equation must be positive, i.e.  $n$  must satisfy the condition  $\text{Re}(n) > 0$ . Hence, the subsequent constraints on the polynomial coefficients form all the possible conditions for instability, of which at least one must be satisfied. These constraints take the following form:

$$\nabla_\mu < 0 \quad (1.3)$$

$$\nabla_{\text{rad}} > \nabla_{\text{ad}} \quad (1.4)$$

$$\nabla_{\text{rad}} > \nabla_{\text{ad}} + \left(\frac{\phi}{\delta}\right) \nabla_\mu \quad (1.5)$$

where  $\nabla_\mu = d\ln\mu/d\ln P$ ,  $\nabla_{\text{rad}} = (\partial\ln T/\partial\ln P)_{\text{rad}}$  and  $\nabla_{\text{ad}} = (\partial\ln T/\partial\ln P)_{\text{ad}}$  are the temperature-pressure gradients for the local environment (dominated by ra-

diation pressure) and the bubble (treated as an adiabatic ideal gas), respectively,  $\phi = (\partial \ln \rho / \partial \ln \mu)_{P,T}$  and  $\delta = -(\partial \ln \rho / \partial \ln T)_{P,\mu}$  (Kippenhahn et al., 1980).

In stellar evolution, the stages described in \*\*\*\* represent extended periods of time in which the stellar interior, described in theoretical models as a series of (quasi-)spherical shells, can be described as being in hydrostatic equilibrium, i.e., the gravitational pressure inwards on material in a given shell, due to the mass enclosed by the shell, is equal to the radiation pressure outwards generated by nuclear fusion occurring within the area enclosed by the shell, either in the core or in an inner shell. Giant stars are objects with luminosities significantly higher and surface gravities lower than stars on the main sequence (which generally have gravities in the range  $4 \lesssim \log(g) \lesssim 5.5$ ).

## 1.4 Previous studies

Cardelli et al. (1989) used observations of bright main-sequence stars to produce empirical equations describing the mean ratio of extinction coefficients at a specific wavelength  $\lambda$  ( $A_\lambda$ ) and the Johnson- $V$  filter ( $A_V$ ), respectively. From this point onward, this ratio will be referred to as  $A_\lambda/A_V$ . They produced a basic universal equation of the form:

$$A_\lambda/A_V = a(x) + b(x)/R_V, \quad (1.6)$$

where  $x \equiv 1/\lambda$  and  $R_V \equiv A(V)/E(B-V)$ . The significance of  $R_V$ , as noted in the same paper, comes from its usefulness as an indicator of the nature of the interstellar medium through which the observed light travels in order to reach the observer.\*\*\*\* The total wavelength range was divided into 4 sub-ranges, each with a governing pair of empirically-determined equations (to determine  $a(x)$  and  $b(x)$ , respectively). This model underpins more recent studies of intrinsic effects on extinction (Girardi et al. (2008), Casagrande & VandenBerg (2018)), and provides the basis for the synthetic  $A_X/A_V$  datasets in this project, \*\*\*\*where  $A_X$  is the coefficient for a given filter  $X$ .

Girardi et al. (2008) produced data tables of  $A_X/A_V$  via bolometric corrections (as was carried out in this study). for stellar atmosphere models with parameters  $T_{\text{eff}}$ ,  $\log(g)$  and  $[\text{Fe}/\text{H}]$ . They carried this out using the same ATLAS9 data Castelli & Kurucz (2004) that was used to generate the data for this project, but also combining it with data from other studies\*\*\*\* Girardi et al. (2002), resulting in data covering a parameter space extending beyond the ATLAS9 limits in all three parameters. They used the data tables to directly\*\*\*\* calculate the  $A_X/A_V$  values for the stellar models in theoretical isochrones\*\*\*\*. While determining that the values of  $A_X/A_V$  varied significantly with  $T_{\text{eff}}$  and  $\log(g)$ , the variation with metallicity was found to be 0.17% between  $[\text{Fe}/\text{H}] = 0.0$  and  $[\text{Fe}/\text{H}] = -2.5$ . They found that, when they set  $A_V = 6$ , there was a systematic shift for the ACS system between extinction values calculated star-wise using the BC tables and a constant extinction value. The constant values of  $A_X/A_V$  were calculated from a yellow dwarf in the low-extinction regime. Overall, the BC tables produced a smaller extinction coefficient in the F814W filter and a

larger (F475W-F814W) colour index value. It also caused a change in the shape of the curve at the MSTO. They then applied the BC table data method to the case of the globular cluster M92. They found the optimal metallicity to be  $Z = 0.0004$  ( $[\text{Fe}/\text{H}] \approx -1.6$ ) instead of the value obtain by previous observers of  $Z = 0.0001$  ( $[\text{Fe}/\text{H}] \approx -2.2$ ). Therefore, their use of BC data caused the estimated cluster metallicity to be greater than when using the standard one-size-fits-all approach to extinction.

\*\*\*\*Casagrande & Vandenberg (2014, 2018a, 2018b) created simple linear models in the \*\*\*\*and Gaia filter systems, expressed for  $R_X = \frac{A_X}{E(B-V)}$ . The equation is independent of surface gravity and has the following form:

$$R_X = a_0 + T_4(a_1 + a_2 T_4) + a_3 [\text{Fe}/\text{H}] \quad (1.7)$$

where  $T_4 = 10^{-4} \times T_{\text{eff}}$ . The equation is valid for  $5250\text{K} \leq T_{\text{eff}} \leq 7000\text{K}$ .

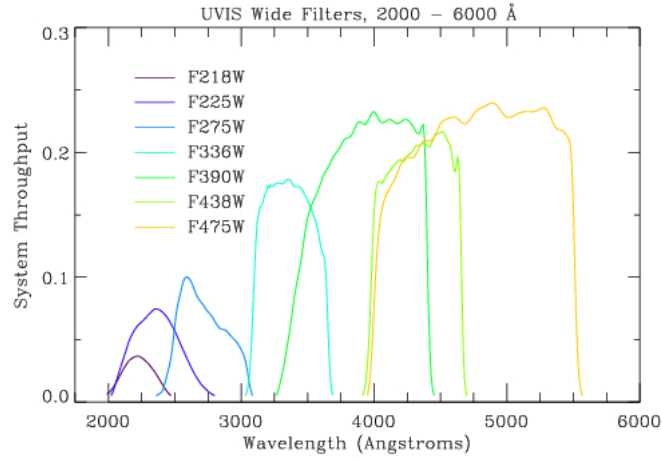


Figure 1.2: Filter response functions for wide-field WFC3 filters. Source: [http://www.stsci.edu/hst/wfc3/ins\\_performance/throughputs/UVIS\\_filterthru.html](http://www.stsci.edu/hst/wfc3/ins_performance/throughputs/UVIS_filterthru.html)

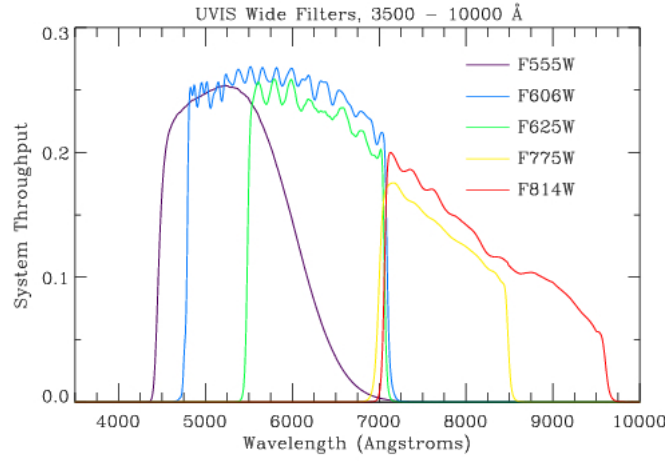


Figure 1.3: Filter response functions for wide-field WFC3 filters. Source: [http://www.stsci.edu/hst/wfc3/ins\\_performance/throughputs/UVIS\\_filterthru.html](http://www.stsci.edu/hst/wfc3/ins_performance/throughputs/UVIS_filterthru.html)

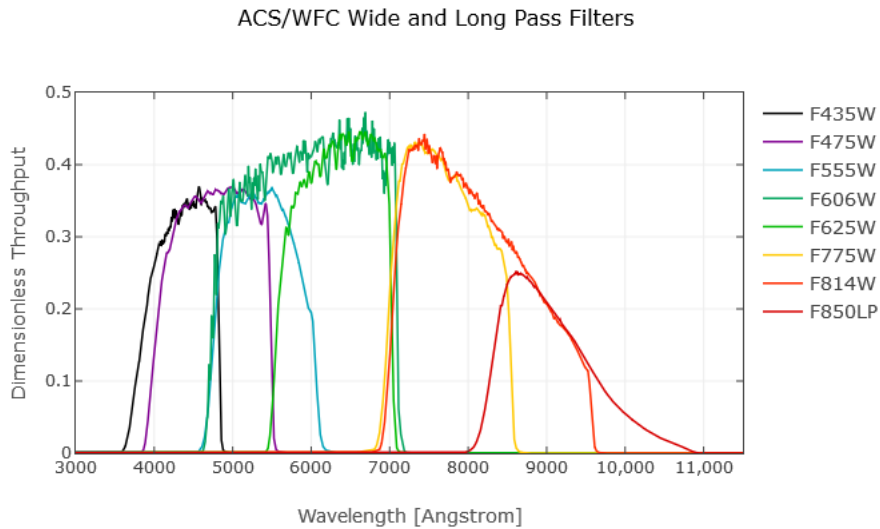


Figure 1.4: Filter response functions for wide-field ACS filters. Source: <http://www.stsci.edu/hst/acs/analysis/throughputs>

# Chapter 2

## Theoretical background

This chapter details the mathematical framework of the physics underpinning this project.

### 2.1 Stellar parameters

To understand the significance of differences between stars with respect to interstellar extinction, we must first define the fundamental features of a stellar atmosphere, which will be used in this project as the input variables on which any star-wise variations in extinction will be modelled.

The effective temperature ( $T_{\text{eff}}$ ) of a star is defined as the temperature of a black body which produces the same bolometric flux as that produced by the star. This approximation is valid because all stars have been observed to have spectra that closely resemble those of black bodies, with the notable exception of atmospheric absorption lines.

$$L = 4\pi R^2 \sigma_{SB} T_{\text{eff}}^4 \quad (2.1)$$

Effective temperature has an effect on interstellar extinction due to its strong effect on the stellar luminosity and, hence, the flux. For a higher flux, more photons are likely to interact with the ISM, hence a higher extinction coefficient.

The metallicity of a star is defined as the fractional abundance of heavy elements, often approximated by iron (Fe) alone, relative to the star's hydrogen (H) abundance, compared to that of the Sun. The abundances are determined by the strength of the elements' characteristic atomic absorption lines in the stellar spectra.

$$[\text{Fe}/\text{H}] = \log \left( \frac{N_{\text{Fe}}}{N_{\text{H}}} \right) - \log \left( \frac{N_{\text{Fe},\odot}}{N_{\text{H},\odot}} \right) \quad (2.2)$$

For a generic atomic species  $E$ ,  $N_E$  represents its number density. For stellar observations,  $N_E$  is measured at the surface. Since the output is logarithmic, a value of  $[\text{Fe}/\text{H}] = 0$  indicates solar metallicity. An increase in metallicity would cause the

corresponding absorption lines to be stronger, thus reducing the observable flux. An increased metallicity also implies an increase in abundance of sub-ferrous metals. The presence of more nuclear species, each with unique absorption line configurations, inevitably creates more observable lines, further increasing the apparent extinction in the spectral flux.

The definition of the stellar surface gravity  $g$  is simply the value of the standard Newtonian gravitational acceleration, applied to the stellar surface (the mass is the total stellar mass,  $M_*$ , and the distance is the stellar radius,  $R_*$ ):

$$g = \frac{GM_*}{R_*^2} \quad (2.3)$$

A higher surface gravity represents a surface with a higher atomic number density. This environment produces a shorter mean free path for photons overall, meaning a smaller collision timescale. If the timescale is sufficiently small, the limit provided by Heisenberg's Uncertainty Principle causes an increase in the uncertainty of the energy absorbed by the atomic electron during the interaction with the photon:

$$\Delta E \Delta t \geq \hbar/2 \quad (2.4)$$

This effect, known as “pressure broadening”, causes a symmetrical distribution of absorption energies (and wavelengths) about the normal emission energy for that particular atomic state. This means that an atomic species in a given quantum state is able to absorb photons at a range of wavelengths. When this is applied over an extended massive region, such as a stellar surface, the result is that fewer photons pass through the surface, thereby reducing the surface flux seen by an outside observer.

## 2.2 Extinction definition

Extinction is defined using the standard astronomical system of flux magnitudes. In general, the difference between two flux measurements,  $F_1$  and  $F_2$ , in magnitudes, is expressed as:

$$m_1 - m_2 = -2.5 \log \left( \frac{F_1}{F_2} \right) \quad (2.5)$$

where  $m_1$  and  $m_2$  are the magnitudes for  $F_1$  and  $F_2$ , respectively. However, the flux of a source varies naturally with the distance to the observer (see Equation 1.1). To account for this, the distances to the nearest stars was determined independently of their flux, by their parallax from Earth. The parallax  $p$  of an object is defined by the angular distance the object moves relative to the “fixed” background as the Earth moves a distance of 1AU (the average separation of the Sun and Earth during one complete orbit) perpendicular to the line-of-sight. This allows the distance,  $d$ , to be measured using the geometry of triangles, combined with the small-angle approximation, as:

$$d/\text{pc} = \frac{1}{(p/\text{arcsec})} \quad (2.6)$$

This gives each astronomical object two fundamental flux measurements. These are the apparent magnitude,  $m$ , and the absolute magnitude,  $M$ . The apparent magnitude is the flux magnitude of a source, as observed by the telescope. The absolute magnitude is the projected flux magnitude of the same source if it were to be placed at a distance of 10 parsecs (pc) from the telescope, thus accounting for the natural decrease in flux due to the distance between the source and the telescope. The relation between these quantities if there is zero extinction can be found by combining Equations 1.1 and 2.5:

$$m - M = -2.5 \log \left( \left( \frac{10\text{pc}}{d} \right)^2 \right) = 5 \log \left( \frac{d}{\text{pc}} \right) - 5 \quad (2.7)$$

The quantity  $(m - M)$  is known as the distance modulus, and, . It should be noted that the distance modulus in Equation 2.7 does not include extinction. To link the apparent magnitude to extinction, it is necessary to separate the distance modulus from the observed apparent magnitude,  $m_{\text{obs}}$ . This can be done by defining the intrinsic apparent magnitude,  $m_0$ , such that:

$$m_0 - M = 5 \log(d/\text{pc}) - 5 \quad (2.8)$$

i.e., the distance modulus is solely dependent on the distance to the sources. Therefore, the extinction  $A$  can be defined as:

$$A = m_{\text{obs}} - m_0 \quad (2.9)$$

This fits with the definition of interstellar extinction given earlier, i.e. as the flux lost solely due to scattering and absorption in the interstellar medium.

However, as noted earlier, in astronomy it is infeasible to attempt observations by a single instrument at all wavelengths. Telescopes instead are generally purpose-built to study a single, relatively narrow wavelength range of the EM spectrum. Within this range, telescope observation ranges are further divided by filters or passbands, one of which is placed on their aperture at any given observation time. As shown in Figures 1.4-1.1, any single filter  $X$  has a limited range of wavelengths for which it is able to detect flux. It can also be seen in these figures that the transmittance of the filter changes as a function of wavelength

$$f_\lambda = \frac{2hc}{\lambda^5 \left( \exp \left( \frac{hc}{\lambda k_B T} \right) - 1 \right)} \quad (2.10)$$

The object of this project is to compare different extinction treatments and the subsequent effect on interpretation observational cluster datasets. For any observational set of stars, the stars' extinction coefficients will be completely unknown from

the data alone. In order to compare observational data and theoretical isochrones via color-magnitude diagrams (CMDs), the most convenient format is to add the (theoretical) extinction coefficients to the theoretical dataset magnitudes (i.e., absolute magnitudes). As a result, the quantity from each dataset that is being compared in the CMDs is the absolute magnitude plus the extinction coefficient. If we label this quantity  $M_{\text{ext},X}$  for a given filter, we can define it as:

$$M_{\text{ext},X} = M_X + A_X \quad (2.11)$$

To measure a star's effective temperature, observers compare the star's observed flux in two filters at different wavelengths, typically in the UV-IR wavelength range. This is because a star with a higher effective temperature will be more luminous in every filter than a cooler star at the same position. This creates uncertainty if the distance measurement cannot be obtained independent of photometry. Therefore, observers utilise the colour index, which is defined as the difference between an object's magnitude in each of the two filters. \*\*\*\*If we compare the black body spectra in Figure 2.1, it can be seen that the maximum monochromatic flux of the black body occurs at an increasingly shorter wavelength for increasingly hotter objects. This makes the object look bluer. The relationship between the wavelength at which the monochromatic flux is maximal and the black body temperature is quantified by Wien's displacement law.

The colour index is defined as the flux magnitude in the bluer (shorter-wavelength) filter minus that in the redder filter. For two filters  $X$  and  $Y$ , with  $X$  being bluer than  $Y$ , the colour index of observations made using them is:

$$\begin{aligned} (X - Y) &= m_X - m_Y \\ &= (m_{X,0} - m_{Y,0}) + (A_X - A_Y) \\ &= (X - Y)_0 + E(X - Y) \end{aligned} \quad (2.12)$$

where  $(X - Y)_0$  is the intrinsic colour index of the object and  $E(X - Y) = A_X - A_Y$  is known as the colour excess, but can also be denoted using "reddening". Due to the potential confusion of the term "reddening" between  $A_X$  and  $E(X - Y)$ , the former will be referred to here as the "extinction" or "extinction coefficient" and the latter as the "colour excess". The colour excess represents the effect of extinction on the observed colour index. The colour excess is important because of the prominence of the intrinsic colour index in determining effective temperature. More negative values of  $(X - Y)$  indicate bluer stars, with higher effective temperatures.

The most commonly-used colour index, employed as a reference for most optical observations, is the Johnson  $(B - V)$  index.

\*\*\*\*Flambda is where t,g,z effects come into BC equations!!!



## 2.3 Bolometric corrections

All the equations in Section \*\*\*\*, including those for extinction, are not useful when applied to telescopes, as any filter will only detect a small fraction of the stellar flux across all wavelengths (known as the bolometric stellar flux) that reaches the telescope. The missing information resulting from this observational constraint renders it difficult to determine the interstellar extinction. These constraints much be mitigated before an accurate value of the extinction coefficient can be determined. This mitigation is carried out by employing bolometric corrections.

The use of bolometric corrections requires the detailed knowledge of stellar spectra least susceptible to significant extinction, i.e., nearby stars with high apparent fluxes. Only with complete knowledge of the spectrum from a reference star can the true spectrum of a distant star with unknown extinction be calculated. The spectra of these stars can be computed by using a grid of predicted fluxes from a stellar atmosphere model, the grid being composed of the stellar parameters known to change emission in stellar atmospheres. These are effective temperature, surface gravity and metallicity. For all filter systems studied in this project, the nearby bright star Vega ( $\alpha$  Lyr) was used as the reference object. Using Vega as the reference star is the most well-known approach to photometric calibration (Casagrande & Vandenberg, 2014).

After accounting for a general extinction effect on an object's emission, its apparent magnitude in a given filter  $X$  (i.e. wavelength range, which we define as increasing from  $\lambda_1$  to  $\lambda_2$ ) is given by:

$$m_X = -2.5 \log_{10} \left( \frac{\int_{\lambda_1}^{\lambda_2} f_\lambda (10^{-0.4A_{X,\lambda}}) S_\lambda d\lambda}{\int_{\lambda_1}^{\lambda_2} f_\lambda^0 S_\lambda d\lambda} \right) + m_X^0 \quad (2.13)$$

where  $f_\lambda$  represents the monochromatic flux at a given wavelength  $\lambda$  at the observer distance,  $A_{X,\lambda}$  is the extinction value as a function of wavelength,  $S_\lambda$  represents the filter response function and  $f_\lambda^0$  and  $m_X^0$  represent the monochromatic flux and apparent magnitude, respectively, of a known reference object in  $X$ .

To derive the equation linking a bolometric correction with the extinction parameter, we start with the definition of a bolometric correction in a filter  $X$ , which is denoted by  $BC_X$ :

$$BC_X \equiv M_{\text{bol}} - M_X \quad (2.14)$$

where  $M_X$  is the absolute magnitude of the object in  $X$  and  $M_{\text{bol}}$  is its (predicted) absolute bolometric magnitude, defined relative to the Sun using:

$$M_{\text{bol}} = M_{\text{bol},\odot} - 2.5 \log_{10} \left( \frac{4\pi R^2 F_{\text{bol}}}{L_\odot} \right) \quad (2.15)$$

where  $F_{\text{bol}}$  is the bolometric stellar flux at its surface,  $R$  is the stellar radius,  $M_{\text{bol},\odot}$

is the solar absolute bolometric magnitude, which is assumed in this work to have a value of 4.75 and  $L_\odot$  is the solar luminosity, for which a value of  $3.844 \times 10^{33} \text{ erg s}^{-1}$  is used. Bolometric corrections can be expressed as a function of extinction using the universal definition of  $M_X$  in terms of  $m_X$  and the distance  $d$  to the source:

$$M_X = m_X - 2.5 \log_{10} \left( \left( \frac{d}{10 \text{ pc}} \right)^2 \right), \quad (2.16)$$

together with the equation  $f_\lambda d^2 = F_\lambda R^2$ , where  $F_\lambda$  is the monochromatic flux at  $\lambda$  at the stellar surface. This gives the final function for a bolometric correction for filter  $X$ :

$$\begin{aligned} BC_X = M_{\text{bol},\odot} - m_X^0 - 2.5 \log_{10} \left( \frac{4\pi R^2 F_{\text{bol}}}{L_\odot} \right) \\ + 2.5 \log_{10} \left( \frac{\int_{\lambda_1}^{\lambda_2} F_\lambda (10^{-0.4A_{X,\lambda}}) S_\lambda d\lambda}{\int_{\lambda_1}^{\lambda_2} f_\lambda^0 S_\lambda d\lambda} \right) \end{aligned} \quad (2.17)$$

For a filter  $X$ , the extinction parameter  $A_X = A_{X,\lambda}$  must be calibrated relative to a known value. In this work we will input a value of the extinction in the well-studied Johnson- $V$  filter,  $A_V$ . To extract  $A_X$ , we use the simple relation:

$$A_X = \left( \frac{A_X}{A_V} \right) A_V \quad (2.18)$$

together with the chosen value of  $A_V$  (for this project the values were  $A_V = 0, 1$  - note that  $BC_X(A_V = 0)$  effectively assumes no extinction in any filter, via Equation ), before taking the difference between the two  $BC_X(A_V)$ , giving the following equation:

$$BC_X(0) - BC_X(A_V) = 2.5 \log_{10} \left( \frac{\int_{\lambda_1}^{\lambda_2} F_\lambda S_\lambda d\lambda}{\int_{\lambda_1}^{\lambda_2} F_\lambda (10^{-0.4(A_{X,\lambda}/A_V)A_V}) S_\lambda d\lambda} \right) \quad (2.19)$$

\*\*\*\*average over the wavelength interval  $[\lambda_1, \lambda_2]$  which is a valid assumption (Casagrande & VandenBerg, 2014), as the CCM relations, which were derived using data from stars observed in the Johnson broad-band filters, themselves were. Due to the nature of the filters' bandpasses, the CCM relations overestimate the extinction in the near-IR and blue-visible Johnson filters\*\*\*\*

## 2.4 Forbes effect

The Forbes effect occurs as a broadband beam of light, such as that passes through an extended partially-transparent medium, such as a series of glass plates, the Earth's

atmosphere or an interstellar gas cloud. It states that the greater the distance travelled by a light beam through the medium, the more penetrating the beam becomes (Forbes, 1842). If we use the case of the glass plates as an example, this means that the fraction of the light incident on the  $n$ th plate in the series which is separated by that plate from the original path is always greater than the corresponding fraction at the  $(n + 1)$ th plate. The physical basis for the Forbes effect is that those photons in the original beam with wavelengths that make them the most likely to be absorbed or refracted are separated from the beam earlier. Therefore, as the beam travels through the medium, its constituent photons are progressively less likely to be separated. Since a higher fraction of its photons are retained as the distance through the medium increases, the beam is more penetrating.

The Forbes effect thus has an impact on the non-zero  $A_V$  value used in Equation 2.19 because if a uniform medium is assumed, as here, where  $R_V$  is held constant at the standard diffuse ISM value of 3.1 (Cardelli et al., 1989), a larger  $A_V$  value implies a longer path through the ISM, and thus a stronger Forbes effect. According to Girardi et al. (2008), any \*\*\*significant impact from the Forbes effect on the values of  $A_X/A_V$  occurs for a chosen  $A_V \gtrsim 4$ . They found that the effect was particularly strong for stars with  $T_{\text{eff}} \lesssim 3000\text{K}$  and that, unsurprising, it became greater as the wavelength range covered by the filter response function increased. The choice of  $A_V = 1$  made for this project should avoid serious problems from the Forbes effect, even for the widest filters.

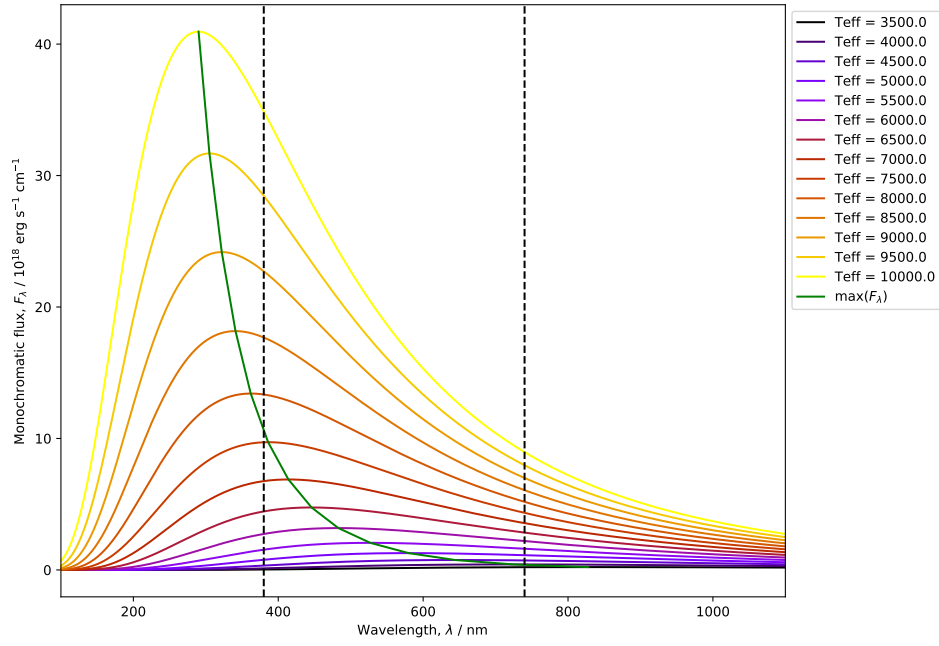


Figure 2.1: \*\*\*\*Monochromatic flux of a black body for different stellar effective temperatures. The black dashed lines mark the approximate limits of the visible part of the EM spectrum. The green curve represents the distributed of the maxima for the other curves.

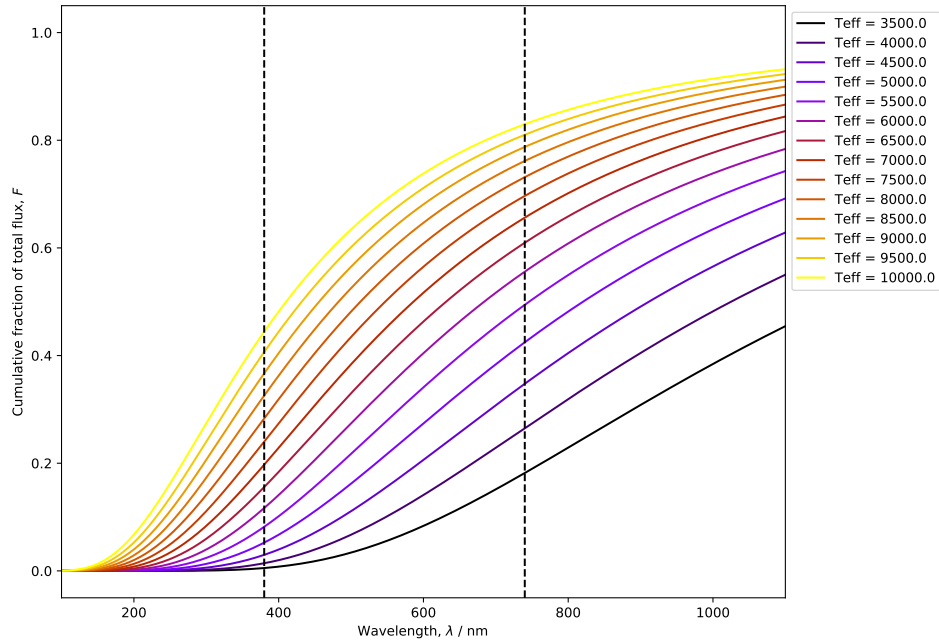


Figure 2.2: Cumulative fraction of the total flux of a black body for different stellar effective temperatures. The black dashed lines mark the approximate limits of the visible part of the EM spectrum.

# Chapter 3

## Methodology

### 3.1 Software used

To generate the predicted stellar flux, the ATLAS9 model stellar atmosphere code (Kurucz, 1993) was used to produce monochromatic fluxes for a series of wavelengths ranging from 9 nm to 160,000 nm, with a resolution of 2 nm or less in the UV. Table 1 of Castelli & Kurucz (2004) contains precise details of the coverage in  $(T_{\text{eff}}, \log(g))$  parameter space, while a brief summary of the limits of the space is listed in Table 3.1. Four input metallicities were used for ATLAS9, at values of  $[\text{Fe}/\text{H}] = -2, -1, 0$  and  $0.5$ , covering the metallicities of most observed globular and open clusters.

The tables of bolometric corrections were generated using a FORTRAN 77 code incorporating the steps described in Section 2.3, inputs with tables describing the response functions of all three filter systems at the same wavelengths as those listed in the ATLAS9 model atmosphere tables, with the number of tables for each stellar metallicity value equal to the total number of  $(T_{\text{eff}}, \log(g))$  combinations available.

Once the bolometric correction tables were produced, all subsequent processes were written in Python 2.7 in the form of IPython notebooks. The repository containing all data, plots and programme codes for this project can be found at [https://github.com/AlexlwAstro/phd\\_work](https://github.com/AlexlwAstro/phd_work).

The isochrones used were generated using the latest Bag of Stellar Tricks and

Parameter / unit	Minimum	Maximum	Number of values
$T_{\text{eff}} / \text{K}$	3500	50000	76
$\log(g / \text{cm s}^{-2})$	0.0	5.0	11
$[\text{Fe}/\text{H}]$	-2.0	0.5	4

Table 3.1: Ranges for the input parameters for ATLAS9 atmospheric models

Isochrones (BaSTI) web interface (Pietrinferni et al. (2004), Hidalgo et al. (2018)). The filter systems whose throughput data were employed by BaSTI to generate the fluxes for the isochrones were ACS, WFC3 and Gaia-DR2. It should be noted that the WFC3 isochrone output does not include flux magnitudes for the F300X filter.

## 3.2 Extinction data

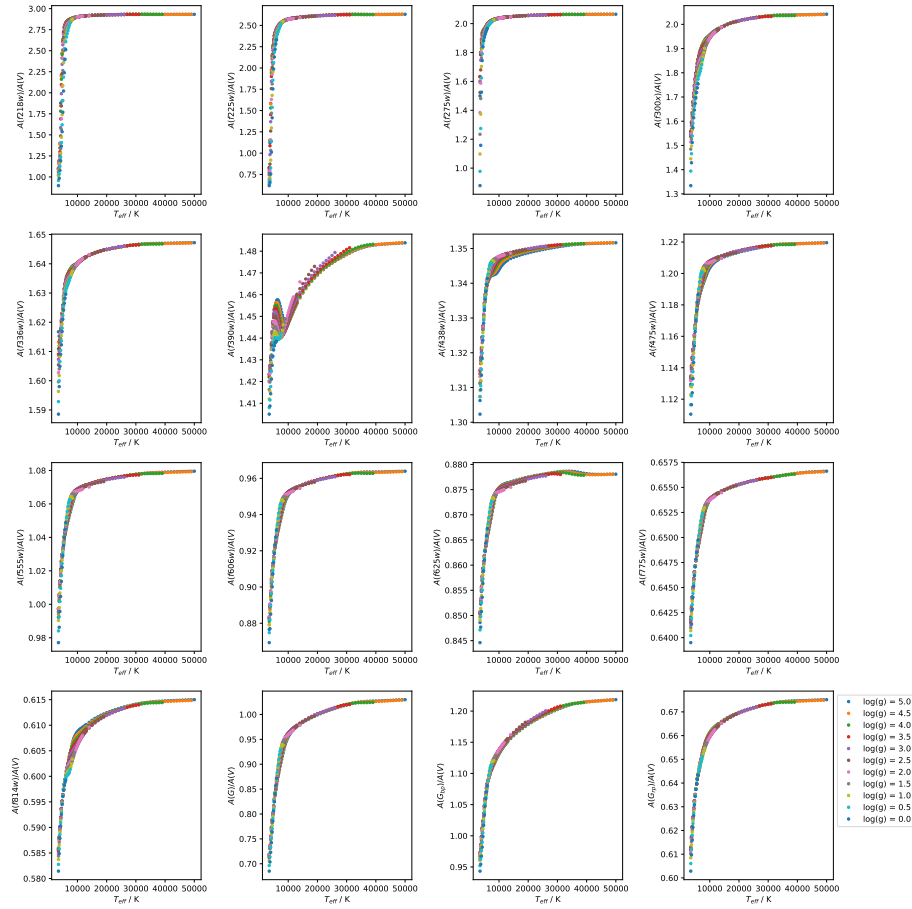


Figure 3.1: WFC3 and Gaia filter  $A_X/A_V$  data for  $[\text{Fe}/\text{H}] = -2$ , plotted against effective temperature, with each colour of dots representing a different value of  $\log(g)$ .

When calculating the bolometric corrections, the reference values taken by the parameters for Vega were:

1.  $m_X^0 = 0.03$  for the Gaia filters
2.  $m_X^0 = 0.00$  for the Hubble WFC3 filters

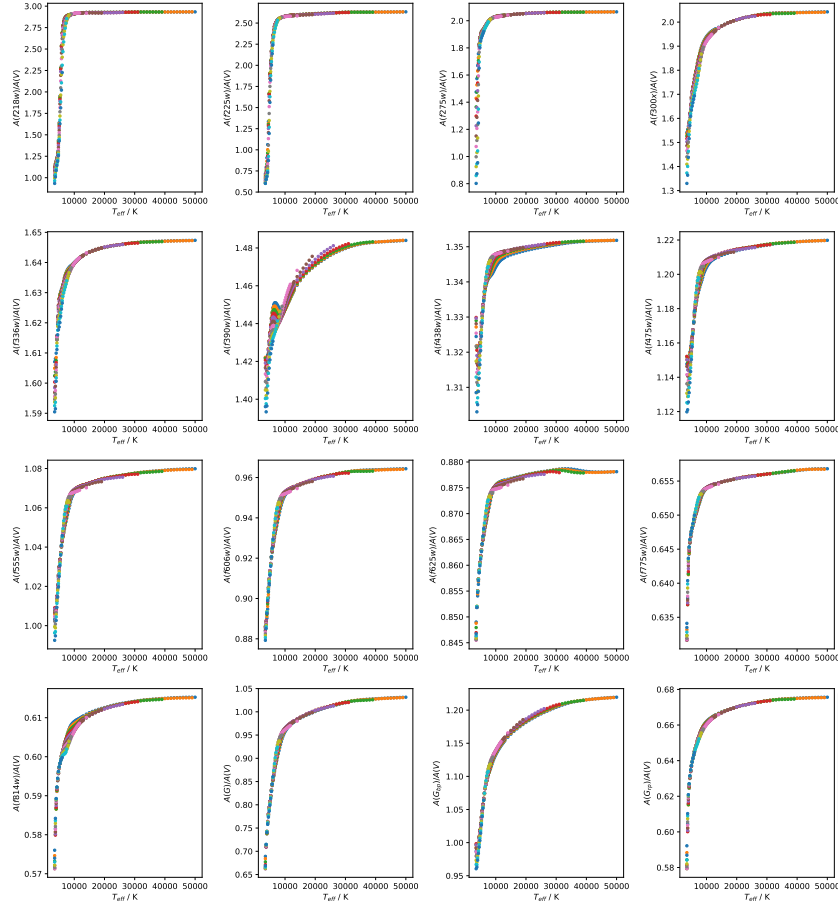


Figure 3.2: WFC3 and Gaia filter  $A_X/A_V$  data for  $[\text{Fe}/\text{H}] = 0.5$ , plotted against effective temperature, with each colour of dots representing a different value of  $\log(g)$ , showing the prominent presence of the tail-flick phenomenon in some filters.

together with  $M_{\text{bol},\odot} = 4.75$ . The Vega model used in this project assumed  $T_{\text{eff}} = 9550\text{K}$  and  $\log(g) = 3.95$ . The mean extinction law from Cardelli et al. (1989), as shown in Equation 1.6, with its different wavelength regimes for  $a(x)$  and  $b(x)$ , was used with the  $A_V$  calibration values to simulate the extinction parameter in Equation 2.17.  $R_V$  was set to a value of 3.1, the standard value for the diffuse interstellar medium. The integration was carried out by iteratively adding the integrand results at regular small wavelength intervals. The non-zero calibration value of  $A_V = 1$  was chosen, as this allows for significant changes in  $A_X/A_V$  from Equation (2.19), while also being close enough to zero to avoid significant changes in  $A_X/A_V$  due to the Forbes effect (Girardi et al., 2008).

To generate extinction-coefficient ratios  $A_X/A_V$  from the bolometric correction data, Equation 2.19 was used to calculate the differences between the  $\text{BC}(A_V = 0)$

and  $BC(A_V = 1)$  datasets and thereby give a single dataset of mean  $A_X/A_V$  values (Girardi et al. (2008), Casagrande & Vandenberg (2014)).

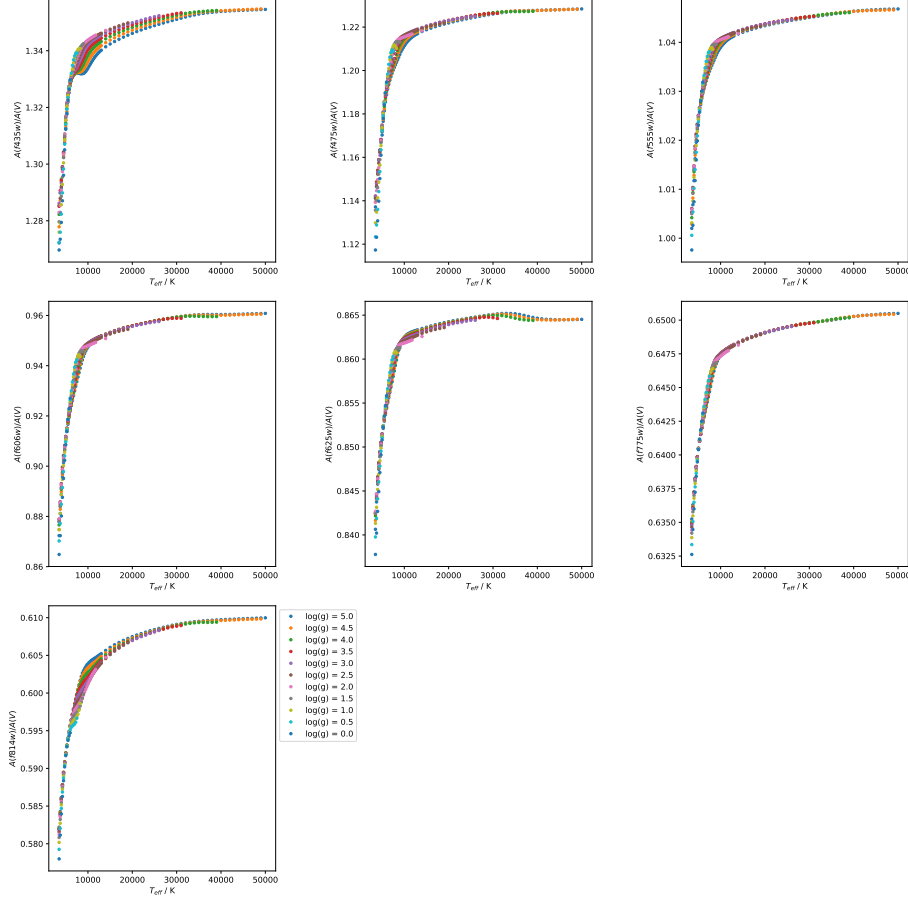


Figure 3.3: ACS filter  $A_X/A_V$  data for  $[\text{Fe}/\text{H}] = -2$ , plotted against effective temperature, with each colour of dots representing a different value of  $\log(g)$ .

As can be seen in the data displayed in Figures 3.1-3.4, in almost all of the filters studied in this project, the longer the central wavelength of a given filter throughput, the smaller the average value of  $A_X/A_V$ , independent of all other parameters. This conforms with the expectation resulting from the fact that the physical mechanisms causing extinction in the ISM preferential affect photons with shorter wavelengths.

Above  $T_{\text{eff}} \approx 12000\text{-}15000$  K, the values of  $A_X/A_V$  are approaching a constant value as a function of all three input parameters. This is reflected in the choice of decay functions as the fitting functions for the data. This region of parameter space will be referred to henceforth as the “high- $T_{\text{eff}}$  extinction plateau region” or simply “plateau”.



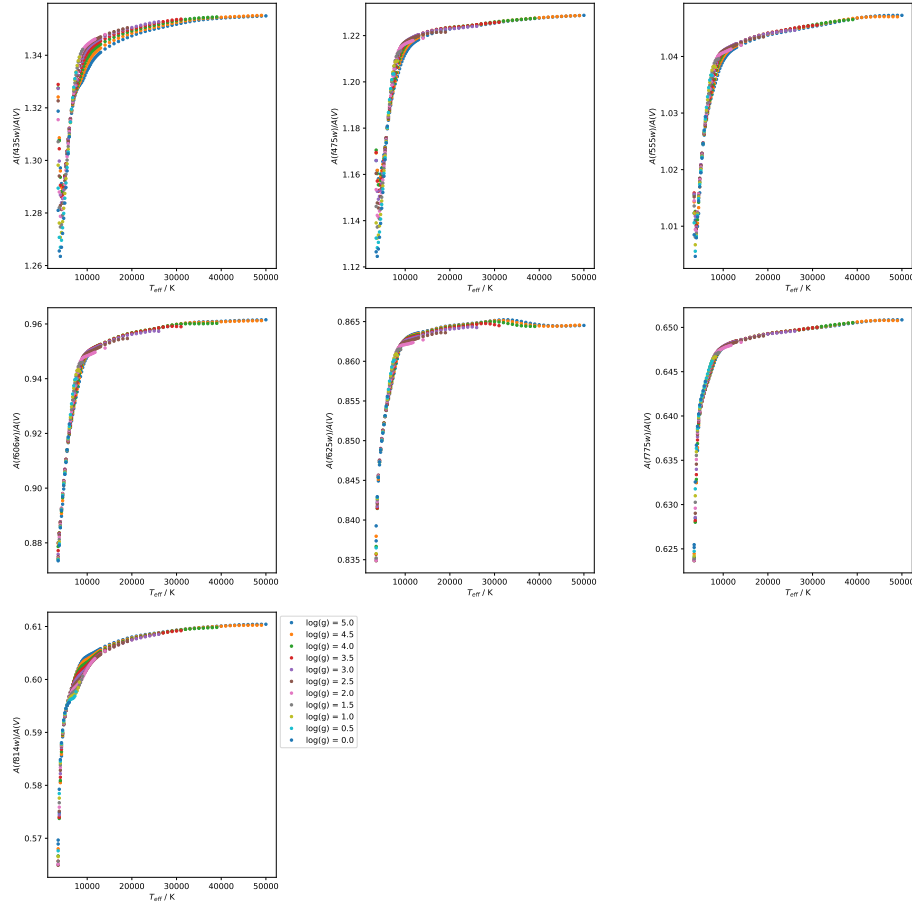


Figure 3.4: ACS filter  $A_X/A_V$  data for  $[\text{Fe}/\text{H}] = 0.5$ , plotted against effective temperature, with each colour of dots representing a different value of  $\log(g)$ , showing the prominent presence of the tail-flick phenomenon in some filters.

### 3.3 Finding & fitting functions

A property found in the data for some filters, more pronounced at higher metallicity but with a possible slight dependence on surface gravity, is the tendency of the gradient of  $A_X/A_V$  with increasing  $T_{\text{eff}}$  to become significantly less positive at the lowest temperatures in the data, typically 4000K and below. The spread in  $A_X/A_V$  values for different  $\log(g)$  is typically about 0.2-04, with a linear progression from  $\log(g) = 5.0$  at the lowest end to  $\log(g) = 0.0$  at the highest. In some filters, at the highest metallicity employed ( $[\text{Fe}/\text{H}] = 0.5$ ), this phenomenon causes the gradient to invert and become significantly negative, reversing the trend everywhere else in the data, including for the same filters at lower metallicity. Due to the shape of the resulting point-to-point line in these axes, it has been dubbed the “tail-flick” phenomenon. This was ignored as an artefact from the numerical integration required for Equation 2.17. This was due to the physical infeasibility of a cooler star experiencing a higher extinction  $A_X$  for a

globally-constant  $A_V$  value and metallicity, as was assumed for data in each BC table. In the relevant filters, only effective temperatures above those affected by the gradient inversion was used for fitting.

In order to find usable functions without running into issues with degeneracy between coefficients, the three input stellar parameters prioritising which parameters to model first, before expanding the function to include parts modelling the impact of other parameters and their associated coefficients. Too many coefficients created errors that were significantly greater in degenerate coefficients than in non-degenerate ones. This would obscure any useful information about the validity of the function form.

The bolometric flux of a black body can be calculated as the total area under the curve described by the Planck function per unit wavelength/frequency as a function of wavelength/frequency. Since stellar emission spectra can be reasonably approximated by a black body emission with absorption lines, it can be seen from Equation 2.1 that the greatest effect on stellar spectra, and therefore on the extinction coefficient, will come from effective temperature. Therefore, the initial functions to be fitted were simple analytical functions of  $T_{\text{eff}}$  only:

$$A_{\text{pow}}(T_{\text{eff}}) = a(T_4)^b + c \quad (3.1)$$

$$A_{\text{exp}}(T_{\text{eff}}) = a \exp(bT_4) + c \quad (3.2)$$

where  $T_4 = 10^{-4} \times T_{\text{eff}}$ . The fitting operation was carried out on the data for solar metallicity ( $[\text{Fe}/\text{H}] = 0.0$ ) and, because it gave the greatest number of  $T_{\text{eff}}$  data points,  $\log(g) = 5$ . This dataset will be referred to as the basic fitting data (BFD).

For the data in the Gaia filters, the opportunity was taken to compare the model for  $R_X$  and coefficients detailed for these filters by Casagrande & Vandenberg (2018). To apply their model to the extinction ratios used for this project, the definition of  $R_X$  was used to construct the following equation:

$$\frac{A_X}{A_V} = \frac{R_X}{R_V} = \frac{R_X}{3.1} \quad (3.3)$$

There were filters whose BFD could not support an accurate fit or maintain the desired accuracy across all combinations of  $\log(g)$  and  $[\text{Fe}/\text{H}]$  using  $A_{\text{pow}}$  or  $A_{\text{exp}}$ . For these filters, more intricate functions were sought, including functions with explicit dependences on  $g$  and  $[\text{Fe}/\text{H}]$ . Several unsuccessful approaches were made before an acceptable function was found for each filter.

The most successful approach was plotting all the available data for each filter, in multiple 2D and 3D axes, and analysing it visually. The trends seen in the data were transcribed to find not only an overarching function template, akin to the status of  $A_{\text{pow}}$  and  $A_{\text{exp}}$ , but also smaller mathematical constructs within the template, such

as describing a decay coefficient in terms of  $\log(g)$  and  $[\text{Fe}/\text{H}]$ . The details of the final form of the template as a function of each stellar parameter were deduced by fitting a logistic function of  $T_{\text{eff}}$  to the  $A_X/A_V$  data for each  $([\text{Fe}/\text{H}], \log(g))$  combination. This was decided on the basis that  $A_{\text{exp}}$  had been superior to  $A_{\text{pow}}$  in describing the data for all relevant filters and because, for these filters, the low- $T_{\text{eff}}$  change in gradient appeared to be more significant than for others and the gradient was not inverted, as can be seen in Figures 3.2-3.3. This is still the case, even after accounting for the difference in  $A_X/A_V$  scale between filters. In particular, the  $T_{\text{eff}}$  gradient prior to the plateau appears to lead to an asymptote at lower, but still physically-viable, temperatures. This issue is resolved by the logistic function's property of converging to a constant value for both very high and low values of the input variable.

For a general logistic function in  $T_{\text{eff}}$ , there are four principle parameters:

- The global maximum value, denoted in this case by  $A_{\text{max}}$ ;
- The global minimum value,  $A_{\text{min}}$ ;
- The exponential decay coefficient,  $k$ ;
- The  $T_{\text{eff}}$ -coordinate of the sigmoid midpoint, in this case  $T_0$ .

It was confirmed that this new function could describe each scenario accurately enough for further analysis. The resulting coefficients were tabulated and analysed for trends and, if found, the nature of those trends. This allowed for the incremental construction of sub-functions of  $\log(g)$  and  $[\text{Fe}/\text{H}]$ , making the overall function,  $A_{\text{logis}}$ , sensitive to all three input stellar atmosphere parameters, with effective temperature having the greatest effect and the relative effects of the other parameters dependent on the best-fit values of the relevant coefficients.

The sub-functions of  $\log(g)$  and  $[\text{Fe}/\text{H}]$ , upon inspection of the coefficients for the  $T_{\text{eff}}$ -only logistic function, were found to be simple functions of  $\log(g)$  and  $[\text{Fe}/\text{H}]$ , independent of  $T_{\text{eff}}$  variations. This allowed for them to be used as the definitions of  $T_0$  and  $k$ , as shown in Equations 3.4 and 3.5, respectively.

$$T_0 = a \log(g) + b \left( \frac{[\text{Fe}/\text{H}]}{||[\text{Fe}/\text{H}]||^{1/2}} \right) + c \quad (3.4)$$

$$k = d \log(g) + e[\text{Fe}/\text{H}] + f \quad (3.5)$$

$$A_{\text{logis}}(T_{\text{eff}}, g, [\text{Fe}/\text{H}]) = \frac{(A_{\text{max}} - A_{\text{min}})}{(1 + \exp(-10^{-4}k(T_{\text{eff}} - T_0)))} + A_{\text{min}} \quad (3.6)$$

The final form was then subjected to a final fit on the entire  $A_X/A_V$  dataset, covering the entire  $(T_{\text{eff}}, \log(g), [\text{Fe}/\text{H}])$  parameter space available.  $A_{\text{logis}}$  was able to accurately reproduce the behaviour of almost the entire dataset. The details are given in Section 4.1.

Isochrone (Age/Myr , [Fe/H])	$T_{\text{eff}}$ minimum	$T_{\text{eff}}$ maximum	$\log(g)$ minimum	$\log(g)$ maximum
500,0.002	2870	9640	0.886	5.137
1000,0.002	2824	8035	1.608	5.184
5000,-1.049	3118	7112	0.456	5.318
10000,-1.049	3086	6412	0.286	5.332

Table 3.2: Ranges of effective temperature and surface gravities in selected BaSTI isochrones

### 3.4 Isochrone data fitting

To obtain isochrones from the BaSTI online database, the desired age range, initial metallicity and filter system must be specified. Therefore, the values of these quantities are shared by all stellar objects. For the stages in stellar evolution prior to the main-sequence turn-off, any changes in atmospheric metallicity are insignificant, due to the factors discussed in Section 1.3.

The output from the BaSTI database for each model stellar object gives the model's initial mass and current mass (i.e. after a time equal to the isochrone age), together with the logarithms of the stellar luminosity in solar units ( $\log(L/L_{\odot})$ ) and of the effective temperature in K ( $\log(T_{\text{eff}})$ ), followed by the absolute magnitudes (with zero extinction) of the object in each filter of the system. To derive the surface gravity  $g$ , we must combine Equation 2.1, to derive the stellar radius, and Equation 2.3. Equation 3.7 shows the resultant definition of  $g$ :

$$g = \frac{4\pi GM_* \sigma_{\text{SB}} T_{\text{eff}}^4}{L_*} \quad (3.7)$$

After this had been completed, each object had a co-ordinate in  $(T_{\text{eff}}, \log(g))$  parameter space, plus the metallicity of the overall isochrone model. The filter magnitudes in the photometric data are the apparent magnitudes of the stars assigned to NGC 6793. Therefore, to match the quantities of the observational and isochrone datasets being compared, it was necessary to correct the observational data for distance and add extinction to the isochrones. This is that standard procedure used when analysing observational data. Thus, we were comparing the  $M_{\text{ext},X}$  values for the isochrones and the observational data. The functions described in Section 3.3 were then applied to the dataset of stellar objects, producing values of  $M_{\text{ext},X}$  for each filter for all objects, as is the standard for analysing observational data with unknown extinction coefficients.

The errors in the parallax data for objects assigned to NGC 6793 were significant, particularly for stars in the lower main-sequence - understandably, since they are the faintest objects in the data and therefore are more difficult to track against the background light sources. This leads to errors in the predicted  $M_{\text{ext},X}$  magnitudes, which is calculated by rearranging Equation 2.7. The significance of the parallax errors in the

main sequence is such that, any differences between isochrones with similar parameters are rendered insignificant. This is the case irrespective of photometric errors in the observed fluxes from the photometric filters.

Since the table for photometric fluxes did not include photometric errors, the parallax errors alone accounted for the total error in the calculated  $M_{\text{ext},X}$ . Therefore, the errors on the flux measurements were exactly equal in all filters for a given star. The errors on the  $(G_{\text{bp}} - G_{\text{rp}})$  color index were calculated as standard, by adding the individual filter errors in quadrature, giving the color errors which were a factor of  $\sqrt{2}$  greater than those for the individual filter fluxes.

When comparing the two approaches to extinction, in order to test for any differences in projected isochrone age via the MSTO, a range of ages must be considered. A “primary” age was utilised as the true cluster isochrone age. This primary isochrone was subjected to both the function-based (FBEC) and standard extinction-coefficient approaches. Two isochrones with ages equidistant from the primary were subjected to the standard approach only. All four of the resulting  $M_{\text{ext},X}$  isochrones were plotted together in the four chosen CMD axes, together with the original (zero-extinction) isochrone for visual reference.

This procedure was employed for two values of  $A_X/A_V$  standard fixed extinction treatment. Both were extracted from the ATLAS9 data tables for a  $\log(g)$  value of 5.0 to represent a main-sequence star, highly desirable when comparing MSTO positions. The ATLAS9 metallicity chosen for calculating these  $A_X/A_V$  values was that which best matched the metallicity of the isochrone to which the coefficient was applied. The ATLAS9 value will be denoted  $[\text{Fe}/\text{H}]_{\text{CM}}$ . The first value was equal to  $(A_X/A_V)_{\text{plat}} = (A_X/A_V)(T_{\text{eff}} = 50,000\text{K}, \log(g) = 5.0, [\text{Fe}/\text{H}]_{\text{CM}})$ , and the second was equal to  $(A_X/A_V)_{\text{MS}} = (A_X/A_V)(T_{\text{eff}} = 5,000\text{K}, \log(g) = 5.0, [\text{Fe}/\text{H}]_{\text{CM}})$ . This was done to reflect the fact that, on one hand, the assumption of a constant extinction coefficient is valid in the plateau region and, on the other, given the position of the MSTO in terms of stellar model  $T_{\text{eff}}$  values, it would be more prudent to ensure that the upper main sequences resulting from both approaches to extinction coincide in the CMD, making it easier to see any disagreements in the turn-off ages. For each of these plots,  $A_V$  was fixed at a value of 1.0.

Given the large number of filters studied in this project, four commonly-used CMD axes were selected to test for any effects of a function-derived  $A_X$ . Two of these are specific to the WFC3 system, with one CMD each for ACS and Gaia.

Cluster property	K05	GC18
Distance modulus / mag	10.73	8.894
-> distance / pc	1400	601
log(age / yr)	8.64	8.78
-> Age / Myr	437	603
$E(B - V)$ / mag	0.17	0.272
$[Fe/H]$	?	?
Members	? (> 3 ACSS-2.5)	465 (271 with Gaia photometry)

Table 3.3: Observational parameters for NGC 6793, according to Kharchenko et al. (2005) (WEBDA archive page) and Gaia Collaboration et al. (2018)

### 3.5 Observational test case: NGC 6793

To test the effects of the difference in treatment of  $A_X/AV$  on observational data, both cases were employed to predict the isochrone parameters (age,  $[Fe/H]$  and  $A_V$ ) of the open cluster NGC 6793.

NGC 6793 has little information available in the literature when compared to open clusters. Two observational studies have been published which give estimates for the properties of the cluster. Both sets of results are listed in Table 3.3.

The Gaia DR2 dataset for NGC 6793, containing the parallaxes and apparent magnitudes (in all three Gaia filters) for 338 objects identified as belonging to the cluster, was obtained. The number of objects is greater than the 271 photometric Gaia objects found by Gaia Collaboration et al. (2018). In addition to this, there were significant variations in the observed parallaxes of individual stars, far beyond the maximum cluster radii expected (Schilbach et al. (2006)). Some objects were even assigned negative parallax values, which are therefore mathematically impossible. Restrictions on the parallax measurements were implemented, by imposing a distance-based selection range centred at 600 pc, which was treated as the centre of the cluster, in line with the Gaia Collaboration et al. (2018) estimate in Table 3.3. The range was decreased until the remaining sample size was approximately equal to 271. When this was implemented, the final sample of observational data for NGC 6793 contained 274 objects. Some of these objects still had parallax distances further from the cluster centre than would be expected for any star cluster. The size of the final dataset balanced the need for maintaining sufficient data points, to achieve a valid comparison to the previous studies of NGC 6793, and eliminating anomalous data.

The isochrone fitting to the NGC 6793 was done by eye using a plot of the cluster's observed Gaia CMD, the position of each star corrected for its parallax distance. Using the values of  $E(B - V)$  and age from Gaia Collaboration et al. (2018), a standard-case isochrone was derived, again assuming a diffuse ISM (i.e.,  $R_V = 3.1$ ). The standard treatment was employed twice, creating a different isochrone each time. A coeffi-

cient calculated from  $(A_X/A_V)_{MS}$  was applied in one case and one calculated using  $(A_X/A_V)_{plat}$  in the other. The fitting process was carried out in sequential stages:

1. First, the upper main sequence of the FBEC isochrone was fitted to that of the standard-case isochrone by varying the value of  $A_V$  used to calculate the final FBEC value for each stellar object.
2. Next, the age of the FBEC isochrone was varied to match the observed turn-off location in the NGC 6793 data as far as possible.
3. Finally, the FBEC isochrone metallicity was varied in an attempt match the observed lower main-sequence.

The isochrone with the resulting parameters were then plotted alongside two standard-case isochrones, The resulting curves were compared to each other for accuracy with respect to the observational data.

# Chapter 4

## Results and discussion

### 4.1 Extinction coefficient models

The extinction-ratio data for all filters, with the exception of the four fully-UV filters in the WFC3 system, could be accurately modelled by the simplest functions trialled for fitting,  $A_{\text{pow}}(T_{\text{eff}})$  or  $A_{\text{pow}}(T_{\text{eff}})$ .

All the functions are consistent with the general trends predicted by the physics in stellar atmospheres, since the effective temperature has the greatest effect upon the value of  $A_X/A_V$ , with relatively minor differences due to

The  $(A_X/A_V)$  data which underpinned this project was derived using the mean extinction laws prescribed in Cardelli et al. (1989). These equations were derived by studying trends in

### 4.2 Effect on isochrones

?? Given the large number of filters studied in Section 4.1, four commonly-used CMD axes were selected to test for any effects of a function-derived  $A_X$ . Two of these are specific to the WFC3 system, with one CMD each for ACS and Gaia.

#### 4.2.1 ACS

The CMD chosen for the ACS was the F435W-(F435W-F814W) axis combination. This CMD is useful as it pairs the bluest and reddest wide-field filters for the ACS in its colour index, which is the index most likely to distinguish between objects with a large range of effective temperatures, making it useful for modelling the main sequence and MSTO, the two most important CMD components for calculating cluster isochrone ages.



System	Filter	Function ( $A_{\text{pow}}$ or $A_{\text{exp}}$ )	Coefficients		
			$a$	$b$	$c$
ACS	F435W	pow	$-0.0276 \pm 0.0061$	$-0.967 \pm 0.1918$	$1.3613 \pm 0.005$
	F475W	pow	$-0.0235 \pm 0.0042$	$-1.2855 \pm 0.174$	$1.2323 \pm 0.0032$
	F555W	pow	$-0.0089 \pm 0.0034$	$-1.534 \pm 0.3895$	$1.0473 \pm 0.0026$
	F606W	exp	$-0.2295 \pm 0.0361$	$-2.9413 \pm 0.3326$	$0.9591 \pm 0.0017$
	F625W	exp	$-0.0741 \pm 0.0487$	$-3.3839 \pm 1.4339$	$0.8647 \pm 0.0016$
	F775W	exp	$-0.0695 \pm 0.0649$	$-3.8286 \pm 2.0938$	$0.6497 \pm 0.0016$
	F814W	exp	$-0.0909 \pm 0.0438$	$-3.2279 \pm 1.0425$	$0.6086 \pm 0.0016$
WFC3	F336W	pow	$-0.0064 \pm 0.0028$	$-1.8004 \pm 0.4633$	$1.6472 \pm 0.0022$
	F390W	exp	$-0.0763 \pm 0.0061$	$-0.7961 \pm 0.1602$	$1.486 \pm 0.0035$
	F438W	exp	$-0.0839 \pm 0.0284$	$-2.5967 \pm 0.6941$	$1.3507 \pm 0.0017$
	F475W	pow	$-0.0224 \pm 0.0041$	$-1.3107 \pm 0.1793$	$1.2233 \pm 0.0031$
	F555W	exp	$-0.2282 \pm 0.0396$	$-3.0752 \pm 0.3704$	$1.0776 \pm 0.0017$
	F606W	exp	$-0.2271 \pm 0.0368$	$-2.9707 \pm 0.3438$	$0.9622 \pm 0.0017$
	F625W	pow	$-0.0048 \pm 0.0028$	$-1.8035 \pm 0.6184$	$0.879 \pm 0.0022$
	F775W	exp	$-0.0713 \pm 0.0695$	$-3.9365 \pm 2.1978$	$0.6558 \pm 0.0016$
	F814W	pow	$-0.0058 \pm 0.0029$	$-1.7434 \pm 0.5318$	$0.6149 \pm 0.0023$
Gaia	G	pow	$-0.0952 \pm 0.0042$	$-1.2853 \pm 0.043$	$1.044 \pm 0.0032$
	G <sub>bp</sub>	pow	$-0.1258 \pm 0.0081$	$-0.7984 \pm 0.0499$	$1.2562 \pm 0.0069$
	G <sub>rp</sub>	pow	$-0.013 \pm 0.0031$	$-1.6863 \pm 0.2444$	$0.6753 \pm 0.0023$

Table 4.1: Coefficient values produced for each filter via  $A_{\text{exp}}$  or  $A_{\text{exp}}$  fitting, as appropriately labelled. Any filters missing from this table are those with data that could not be accurately fitted using either function.

Filter	Function ( $A_{\text{pow}}$ or $A_{\text{exp}}$ )	Coefficients		
		$a$	$b$	$c$
F218W	exp	$-0.0763 \pm 0.0061$	$-0.7961 \pm 0.1602$	$1.486 \pm 0.0035$
F225W	exp	$-0.0839 \pm 0.0284$	$-2.5967 \pm 0.6941$	$1.3507 \pm 0.0017$
F275W	pow	$-0.0224 \pm 0.0041$	$-1.3107 \pm 0.1793$	$1.2233 \pm 0.0031$
F300X	blah****	$-0.2282 \pm 0.0396$	$-3.0752 \pm 0.3704$	$1.0776 \pm 0.0017$

Table 4.2: Coefficient values for non-trivial functions produced for fitting to UV filter data.

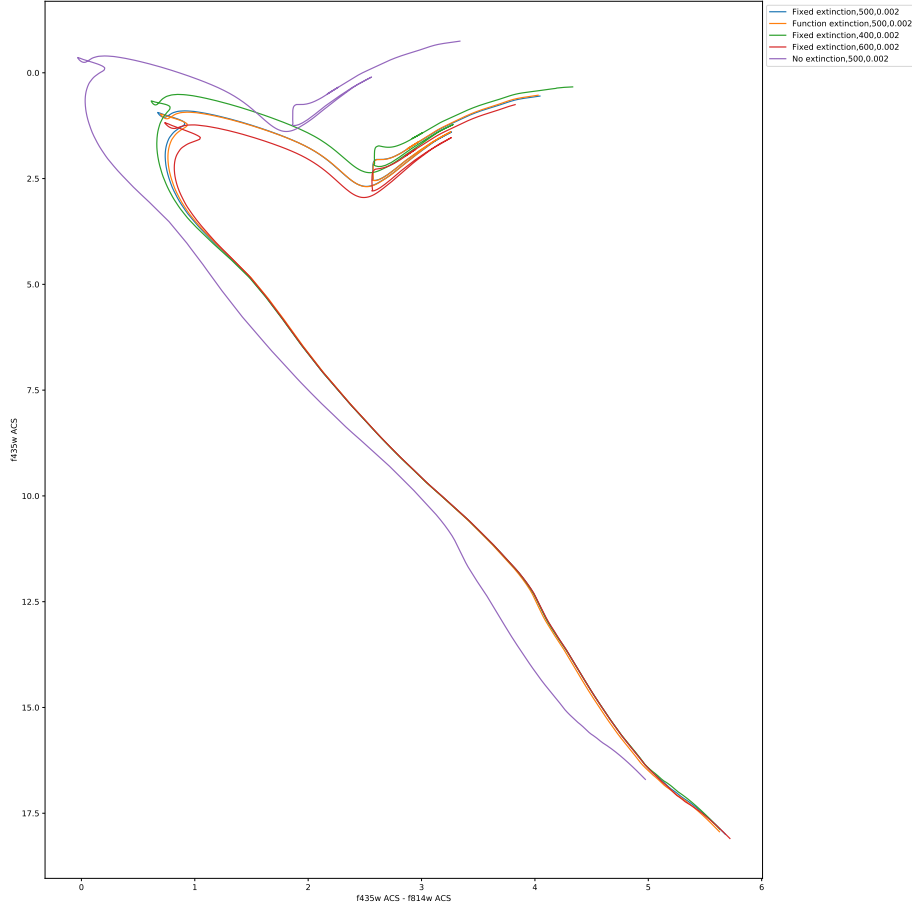


Figure 4.1: ACS F435W-(F435W-F814W) CMD with a fixed extinction coefficient equal to  $(A_X/A_V)_{MS}$  for each filter

### 4.2.2 WFC3

The CMD chosen for the ACS was the F435W-(F435W-F814W) axis combination. This CMD is useful as it pairs the bluest and reddest wide-field filters for the ACS, which produces larger spectral colours.\*\*\*\*

### 4.2.3 Gaia

The photometric filters in Gaia, as shown by their respective response functions in Figure 1.1, are designed such that the only reasonable colour index is the  $(G_{bp} - G_{rp})$  index. The  $G$  filter, being the widest filter of the three available wide-field filters. This CMD is useful as it pairs the bluest and reddest wide-field filters for the ACS, which produces larger spectral colours.\*\*\*\*

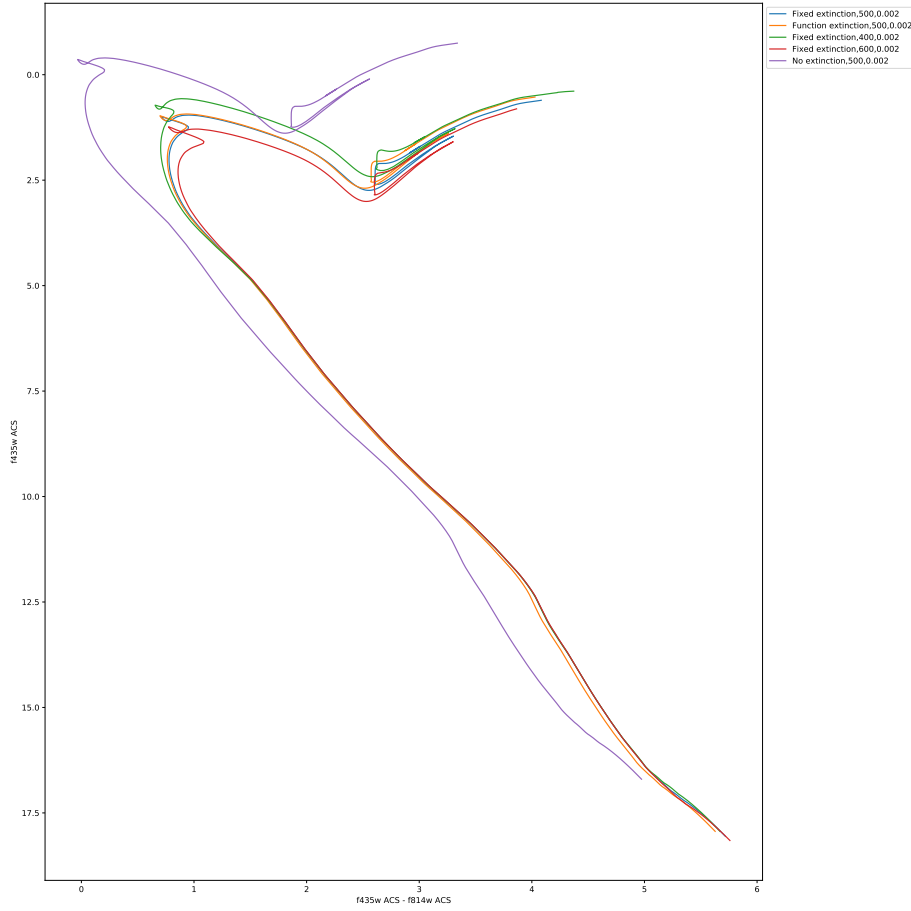


Figure 4.2: ACS F435W-(F435W-F814W) CMD with a fixed extinction coefficient equal to  $(A_X/A_V)_{plat}$  for each filter

### 4.3 NGC 6793

There are highly significant errors for the individual objects in the Gaia data propagation, even when assuming the only source of error is from parallax measurements, as shown in Figure 4.9. The magnitude of the errorbars dwarf any changes in isochrones due to extinction coefficient treatments in the main sequence. For the few objects in the data with

\*\*\*\*Get zoom in on turn-off region

All the isochrones, as shown in Section\*\*\*\*, are sensitive both to the reference extinction coefficient value  $A_V$  and to the value of  $A_X/A_V$  for the fixed-coefficient case, which is to be expected. Some individual parts of the isochrones relevant to this study are additionally sensitive to other isochrone parameters:

1. The position of the MSTO is sensitive to the treatment of  $A_X/A_V$ , as shown in Section\*\*\*\*, and the isochrone age.

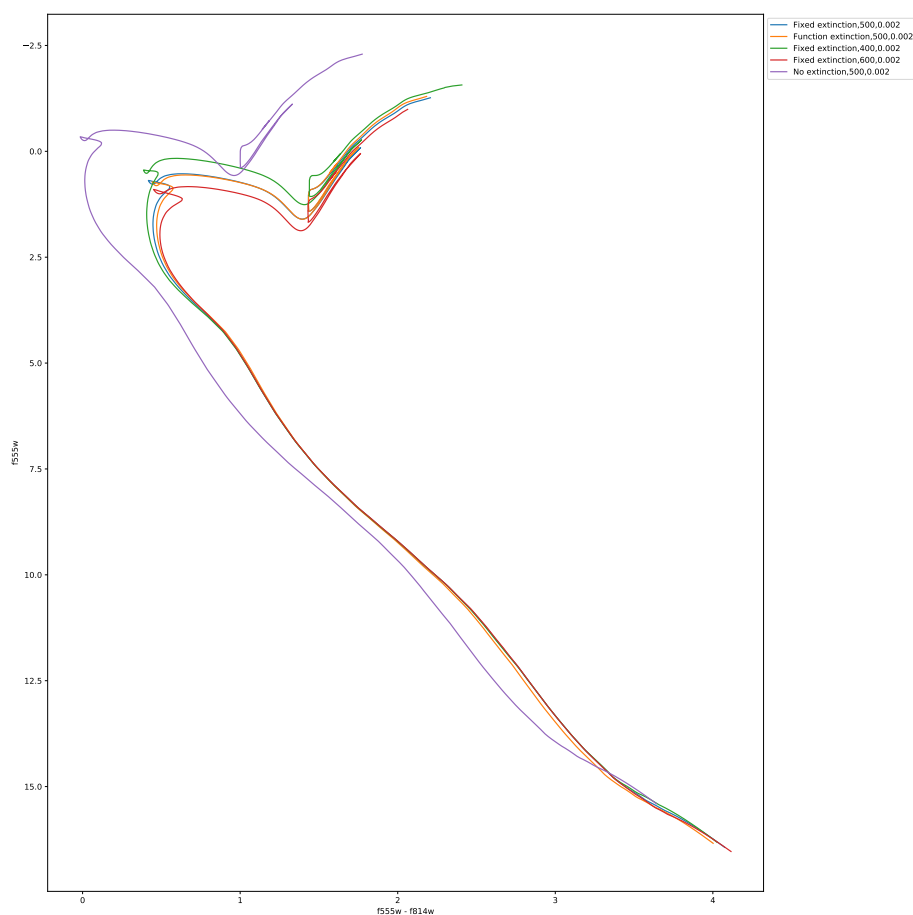


Figure 4.3: WFC3 F555W-(F555W-F814W) CMD with a fixed extinction coefficient equal to  $(A_X/A_V)_{MS}$  for each filter

2. The position of the lower main sequence is significantly more sensitive to metallicity than other parts of the isochrone.

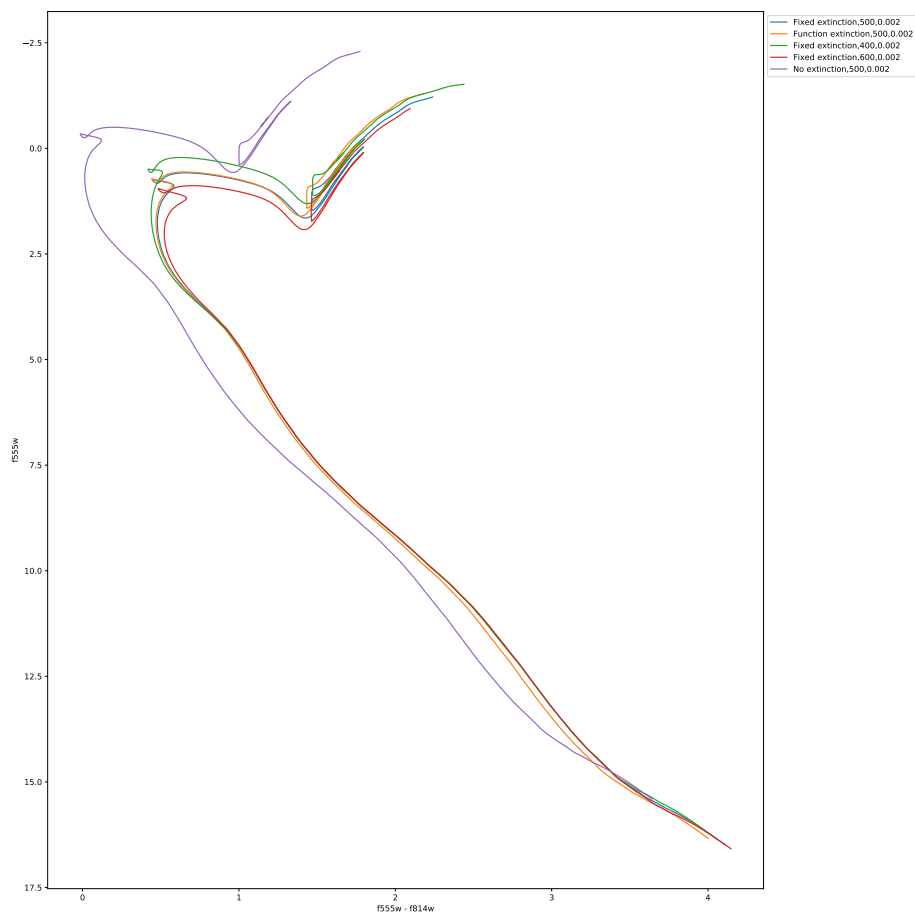


Figure 4.4: WFC3 F555W-(F555W-F814W) CMD with a fixed extinction coefficient equal to  $(A_X/A_V)_{plat}$  for each filter

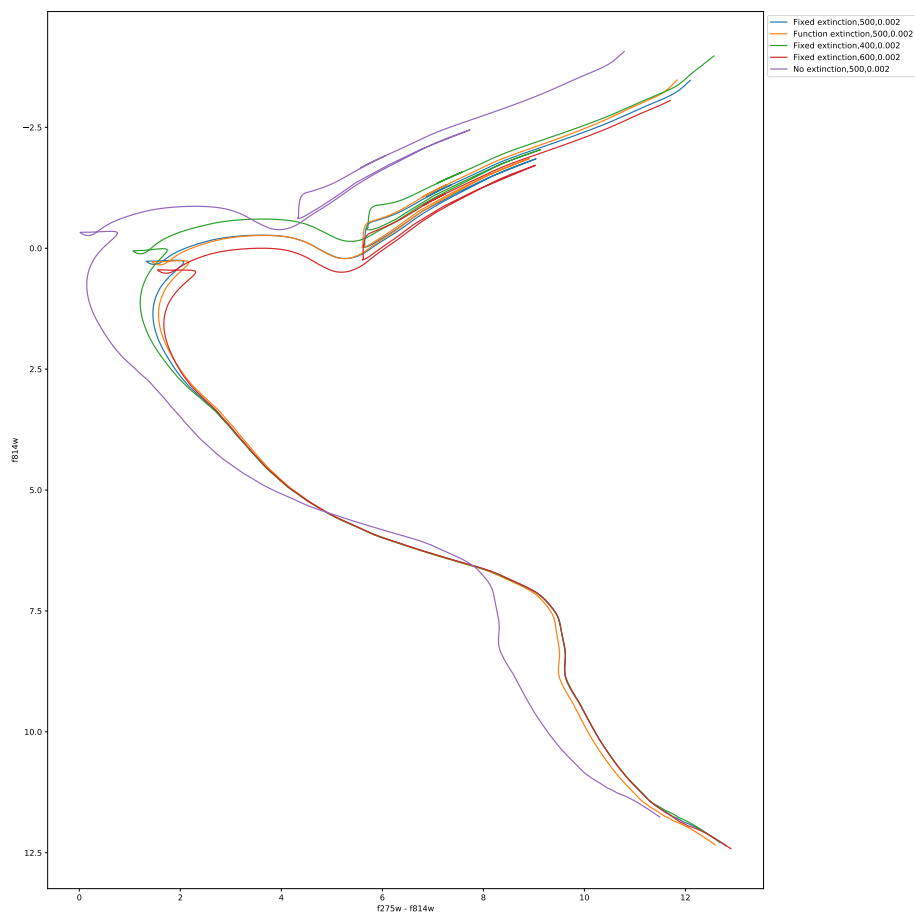


Figure 4.5: WFC3 F814W-(F275W-F814W) CMD with a fixed extinction coefficient equal to  $(A_X/A_V)_{MS}$  for each filter

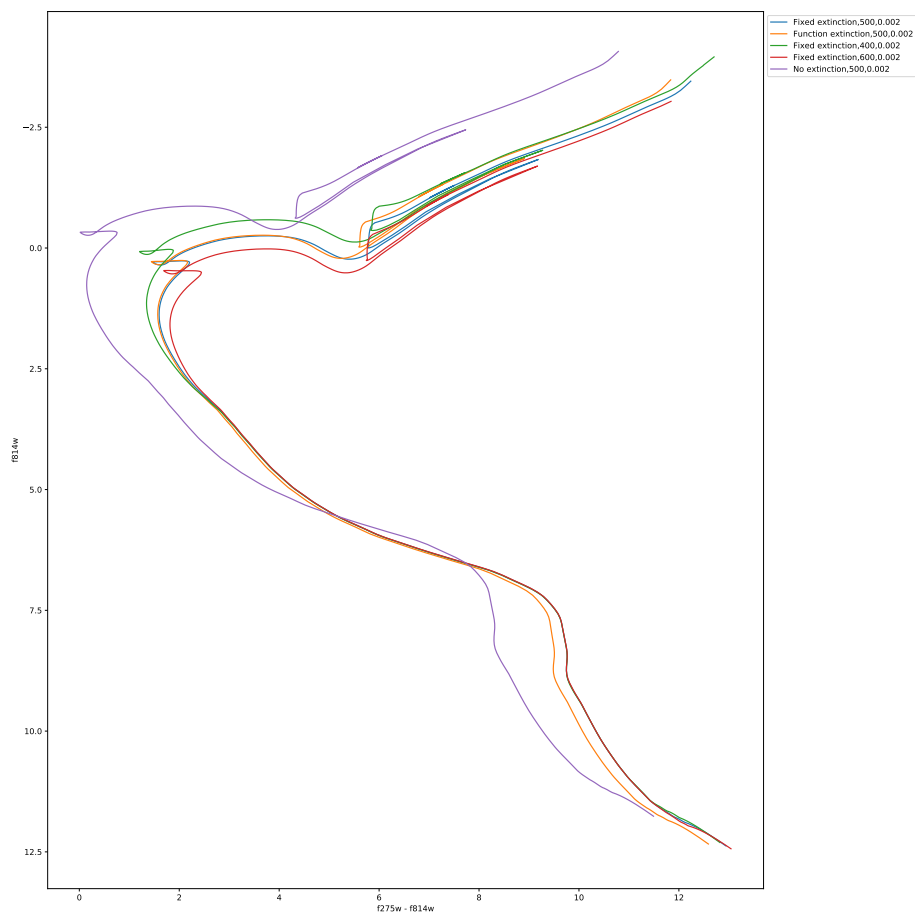


Figure 4.6: WFC3 F814W-(F275W-F814W) CMD with a fixed extinction coefficient equal to  $(A_X/A_V)_{plat}$  for each filter

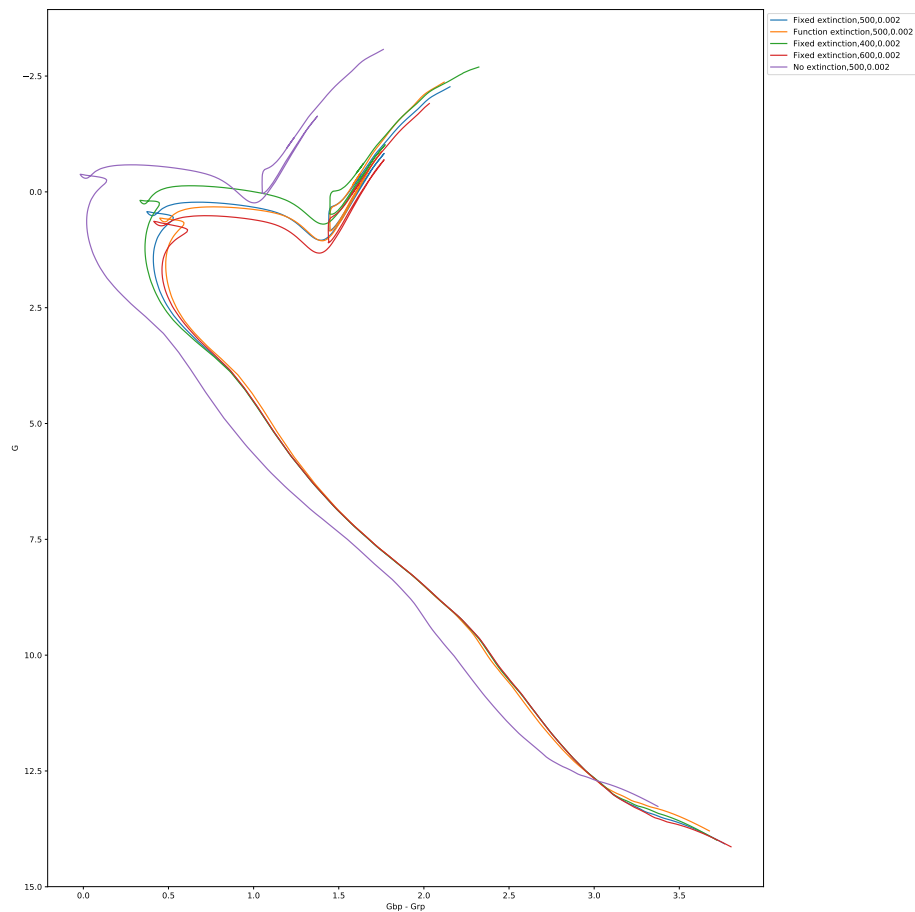


Figure 4.7: Gaia  $G$ -( $G_{bp}$ - $G_{rp}$ ) CMD with a fixed extinction coefficient equal to  $(A_X/A_V)_{MS}$  for each filter



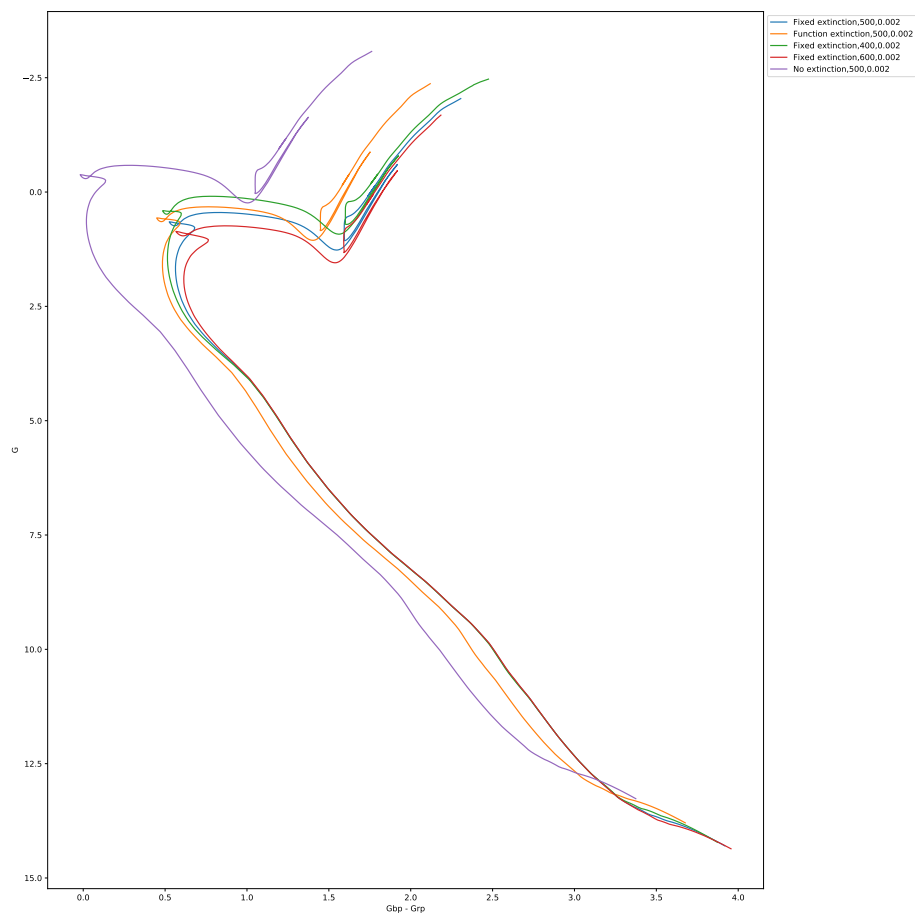


Figure 4.8: Gaia  $G$ -( $G_{bp}$ - $G_{rp}$ ) CMD with a fixed extinction coefficient equal to  $(A_X/A_V)_{plat}$  for each filter

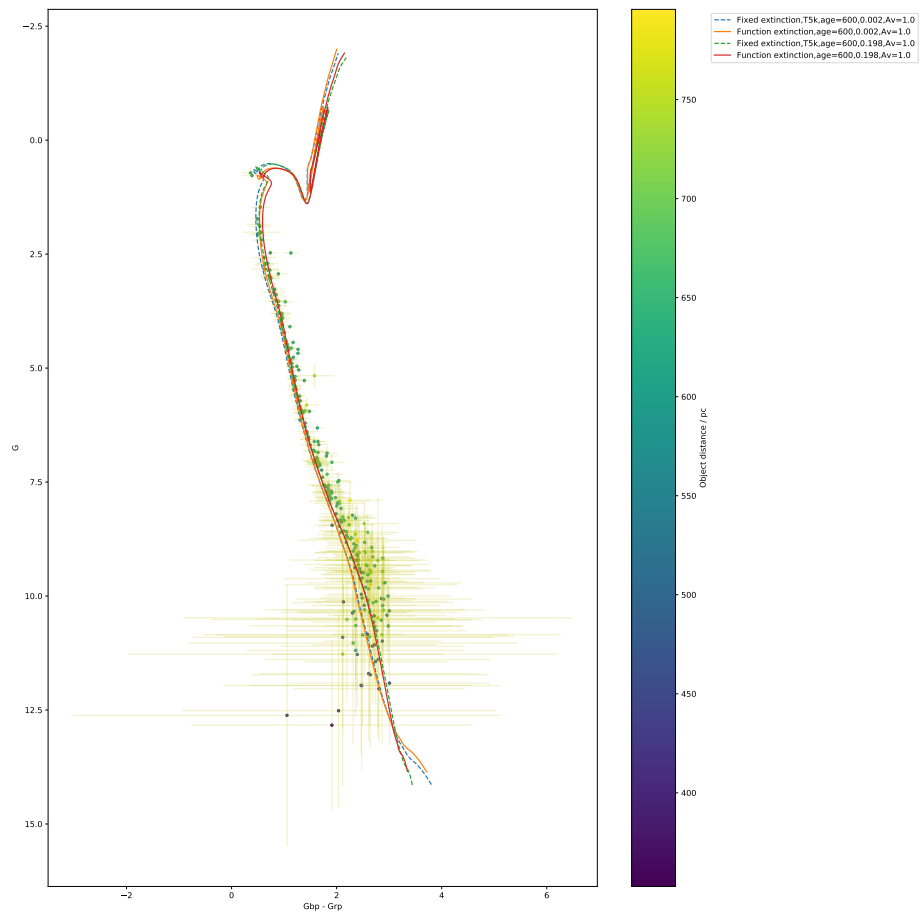


Figure 4.9: Gaia CMD of NGC 6793 with errorbars included.

# Chapter 5

## Conclusion

In all cases, applying a fixed extinction to all points in an isochrone causes the main-sequence turn-off to occur at a more luminous, bluer point in a given CMD than the MSTO point for an extinction coefficient described using a function fitted to empirically derived data.

### 5.1 Future work

# Bibliography

- Baraffe I., Chabrier G., 2018, A&A, 619, A177
- Cardelli J. A., Clayton G. C., Mathis J. S., 1989, ApJ, 345, 245
- Casagrande L., VandenBerg D. A., 2014, MNRAS, 444, 392
- Casagrande L., VandenBerg D. A., 2018, MNRAS, 479, L102
- Castelli F., Kurucz R. L., 2004, ArXiv Astrophysics e-prints
- Forbes J. D., 1842, Philosophical Transactions of the Royal Society of London Series I, 132, 225
- Gaia Collaboration et al., 2018, A&A, 616, A10
- Girardi L., Bertelli G., Bressan A., Chiosi C., Groenewegen M. A. T., Marigo P., Salasnich B., Weiss A., 2002, A&A, 391, 195
- Girardi L., et al., 2008, PASP, 120, 583
- Hidalgo S. L., et al., 2018, ApJ, 856, 125
- Jordi C., et al., 2010, A&A, 523, A48
- Kharchenko N. V., Piskunov A. E., Röser S., Schilbach E., Scholz R.-D., 2005, A&A, 438, 1163
- Kippenhahn R., Ruschenplatt G., Thomas H.-C., 1980, A&A, 91, 175
- Kurucz R., 1993, ATLAS9 Stellar Atmosphere Programs and 2 km/s grid. Kurucz CD-ROM No. 13. Cambridge, Mass.: Smithsonian Astrophysical Observatory, 1993., 13
- Pietrinferni A., Cassisi S., Salaris M., Castelli F., 2004, ApJ, 612, 168
- Salaris M., Cassisi S., 2017, Royal Society Open Science, 4, 170192
- Schilbach E., Kharchenko N. V., Piskunov A. E., Röser S., Scholz R.-D., 2006, A&A, 456, 523